Journal of Materials Science: Materials in Electronics
https://doi.org/10.1007/s10854-018-9139-4

Reduced graphene oxide-multiwalled carbon nanotubes hybrid film with low Pt loading as counter electrode for improved photovoltaic performance of dye-sensitised solar cells

A. B. Suriani[1,2] · Muqoyyanah[1,2] · A. Mohamed[1,3] · M. H. D. Othman[4] · M. H. Mamat[5] · N. Hashim[1,3] · M. K. Ahmad[6] · N. Nayan[6] · H. P. S. Abdul Khalil[7]

Received: 16 February 2018 / Accepted: 19 April 2018

Abstract

In this work, the role of reduced graphene oxide (rGO) with hyperbranched surfactant and its hybridisation with multiwalled carbon nanotubes (MWCNTs) and platinum (Pt) nanoparticles (NPs) as counter electrode (CE) were investigated to determine the photovoltaic performance of dye-sensitised solar cells (DSSCs). Sodium 1,4-bis(neopentyloxy)-3-(neopentyloxycarbonyl)-1,4-dioxobutane-2-sulphonate (TC14) surfactant was utilised as dispersing and stabilising agent in electrochemical exfoliation to synthesise graphene oxide (GO) as initial solution for rGO production prior to its further hybridisation and fabrication as thin film. A chemical reduction process utilising hydrazine hydrate was conducted to produce rGO due to the low temperature process and water-based GO solution. Subsequently, hybrid solution was prepared by mixing 1 wt% MWCNTs into the produced rGO solution. TC14-rGO and TC14-rGO_MWCNTs hybrid solution were transferred into fluorine-doped tin oxide substrate to fabricate thin film by spraying deposition method. Finally, the CE films were prepared by coating with thin Pt NPs. Photoanode film was prepared by a two-step process: hydrothermal growth method to synthesise titanium dioxide nanowires (TiO_2 NWs) and subsequent squeegee method to apply TiO_2 NPs. According to solar simulator measurement, the highest energy conversion efficiency (η) was achieved by using CE-based TC14-rGO_MWCNTs/Pt (1.553%), with the highest short current density of 4.424 mA/cm^2. The highest η was due to the high conductivity of CE hybrid film and the morphology of fabricated TiO_2 NWs/TiO_2 NPs. Consequently, the dye adsorption was high, and the photovoltaic performance of DSSCs was increased. This result also showed that rGO and rGO_MWCNTs hybrid can be used as considerable potential candidate materials to replace Pt gradually.

✉ A. B. Suriani
suriani@fsmt.upsi.edu.my

[1] Nanotechnology Research Centre, Faculty of Science and Mathematics, Universiti Pendidikan Sultan Idris, 35900 Tanjung Malim, Perak, Malaysia

[2] Department of Physics, Faculty of Science and Mathematics, Universiti Pendidikan Sultan Idris, 35900 Tanjung Malim, Perak, Malaysia

[3] Department of Chemistry, Faculty of Science and Mathematics, Universiti Pendidikan Sultan Idris, 35900 Tanjung Malim, Perak, Malaysia

[4] Advanced Membrane Technology Research Centre (AMTEC), Universiti Teknologi Malaysia, 81310 Skudai, Johor, Malaysia

[5] NANO-ElecTronic Centre (NET), Faculty of Electrical Engineering, Universiti Teknologi MARA (UiTM), 40450 Shah Alam, Selangor, Malaysia

[6] Microelectronic and Nanotechnology−Shamsuddin Research Centre (MiNT-SRC), Faculty of Electrical and Electronic Engineering, Universiti Tun Hussein Onn Malaysia, Batu Pahat, 86400 Parit Raja, Johor, Malaysia

[7] Wood, Paper and Coating Division, School of Industrial Technology, Universiti Sains Malaysia, 11800 Pulau, Pinang, Malaysia

Published online: 18 May 2018

1 Introduction

Dye-sensitised solar cells (DSSCs) are third-generation solar cells, which have attracted attention since its invention by O'Regan and Grätzel in 1991 [1]. DSSCs are developed to replace silicon-based solar cell and reduce the usage of fuel or gas for electricity. These cells are used due to their high energy efficiency with low cost and simple fabrication, thereby their potential for industrial fabrication [2]. DSSCs are consisted of four parts: an anode electrode (photoanode) coated with semiconductor layer, a photo sensitiser (dye), an electrolyte-containing redox couple and a cathode electrode [counter electrode (CE)]. The illumination of photon-containing sunlight to photoanode causes the adsorbed dye on semiconductor layer to excite electrons. The excited electrons on semiconductor layer are subsequently transferred to photoanode substrate by diffusion [3], and they move further to the CE substrate. The amount of electrons transferred to CE, known as short current density (J_{SC}), determines the energy conversion efficiency (η) of DSSCs. Accordingly, dye adsorption and electron transfer highly depend on the morphology and crystallinity of semiconductor layer and thin CE film [4, 5].

CE displays an important role in DSSCs by facilitating electron transfer from photoanode to complete the current cycle. Platinum (Pt) nanoparticles (NPs) are common materials used as CE due to their high electrocatalytic activity and electrical conductivity [6]. High η of 12.3% is achieved by using Pt as CE [7]. The utilisation of Pt as CE should be reduced and eventually replaced with other materials because it is an expensive and easily corroded material. Several carbon-based materials, such as activated carbon, single or multiwalled carbon nanotubes (MWCNTs) [8], graphene and graphene oxide (GO) or reduced GO (rGO), were investigated to replace Pt due to their low cost, relatively good electrocatalytic activity and resistance to corrosion [9]. Dobrzanski et al. [10] fabricated MWCNTs CE thin film by using spin coating technique and achieved a η of 5.97%. Moreover, Ramasamy et al. [8] achieved high η of 7.59% when using MWCNTs CE film fabricated by spray coating method. The usage of GO and rGO as CE material either by Hummers' or exfoliation method also presents relatively high η [11–14]. Recently, an η of 4.72% is achieved by using rGO as CE [15]. GO exhibits low η (1.59%) [12] due to its high oxygen functional groups; consequently, the electron transfer resistance increases, and the DSSC performance decreases.

GO synthesis using Hummers' method provides many-step procedures in thin film fabrication due to the powder form of synthesised GO, which needs the addition of dispersing agent. The utilisation of strong acid, toxic chemicals and complex synthesis procedures also restrict and make this method complicated [16]. Electrochemical exfoliation method, which utilises acidic or sulfuric electrolyte, offers a simple GO synthesis procedure and an advantage due to a large-scale production in the solution form from a single-synthesis process [17, 18]. An environment-friendly synthesis by using water as solvent, which is assisted with surfactant for intercalation and stabilisation of graphite layer, provides a low cost and safe procedure. According to previous work [13, 14], the surfactant tail number significantly affects the quality of produced GO. The triple-tail surfactant promotes triple interaction during exfoliation process, thereby producing thinner layer than that of single-tail surfactant. Less agglomeration on the rGO layer is also achieved due to its improved dispersion and stabilisation role on the produced rGO solution. However, η of DSSCs based on GO or rGO CE thin films is relatively lower than that when Pt is utilised as CE. To improve the performance, the hybridisation between carbon-based materials, such as GO- or rGO_MWCNTs, is widely investigated. With their hybridisation, these materials display higher η (6.91%) than that of pristine rGO or MWCNTs film due to the larger surface area and higher electrical conductivity of the former than that of the latter [19]. Nonetheless, η is still lower than that of the conventional Pt CE film (12.3%) [7].

Furthermore, several Pt improvements, such as fabrication method, material modification and hybridisation with other materials, were also performed to achieve high DSSCs efficiency. Song et al. [6] combined urea in Pt fabrication by homogeneous deposition method with subsequent reduction using ethylene glycol; they achieved 9.34% DSSCs efficiency. They also found that small Pt particles highly increase catalytic activity due to the large surface area. Bajpai et al. [20] showed that ~ 27% Pt loading combined with graphene yields higher efficiency (2.91%) than that of ~ 34% Pt loading (~ 2.79%). Therefore, less Pt loading results in increased DSSCs performance when it is hybridised with GO or rGO. Pt hybridisation with carbon-based material is still a subject of investigation to obtain high η.

In the present work, rGO and MWCNTs coated with thin Pt NPs (10 nm) were hybridised to compare the resultant product performance with those of pristine rGO, MWCNTs and Pt NPs film as thin CE film. MWCNTs and rGO were produced using similar procedures in previous study [20–26], in which MWCNTs are produced from waste cooking palm oil (WCPO) as precursor by modified thermal chemical vapour deposition method [28]. In previous works [27–32], WCPO-based MWCNTs were investigated for their use as nanofillers in natural rubber latex with customised hyperbranched sodium 1,4-bis(neopentyloxy)-3-(neopentyloxycarbonyl)-1,4-dioxobutane-2-sulphonate (TC14) surfactant for application in

supercapacitor electrodes. This result showed that the produced WCPO-based MWCNTs can be potentially applied as electrode materials in electronic device. Additionally, rGO is produced by utilising triple-tail TC14 surfactant. The TC14-rGO CE thin film presents higher η than that of rGO film produced by utilising commercially available single-tail sodium dodecyl sulphate surfactant due to its thin and agglomerated free rGO layer produced from triple-tail TC14 surfactant; consequently, the electrolyte diffusibility is enhanced [13, 14]. Hence, in the present work, GO was initially synthesised by using the simple electrochemical exfoliation method with the aid of TC14 surfactant. Chemical reduction process was carried out by adding a small amount of hydrazine hydrate as reducing agent to produce rGO. The fabrication of pristine MWCNTs and TC14-rGO and their hybridisation (TC14-rGO_MWCNTs) were carried out by using the simple and easy controlled spraying deposition method, which is suitable for various sizes and kinds of substrates [33]. CE thin film was subsequently coated with Pt NPs (10 nm) to improve the rGO conductivity and catalytic activity. To the best of our knowledge, this study is the first to report about the utilisation of MWCNTs from WCPO and their hybridisation with TC14-rGO prior to coating with thin Pt NPs as CE thin films for DSSCs application.

The morphology of photoanode material is also important in the photovoltaic performance of DSSCs due its role in dye adsorption, which determines the amount of excited electron. Titanium dioxide (TiO_2) is a widely used and potential semiconductor layer for photoanode. TiO_2 exhibits better performance in DSSCs application than that of zinc oxide (ZnO) [34–36]. The large surface area of TiO_2 NPs results in high dye adsorption. Thus, these NPs are recommended for DSSCs. Recently, 1D TiO_2 nanostructures, such as nanorods (NRs) [3, 37], nanotubes [38] and nanowires (NWs) [5, 39], gain considerable interest for their application as DSSCs photoanode due to their improved light harvesting ability, less grain boundary, slow electron recombination and fast electron transport [5, 40]. TiO_2 NWs perform better than TiO_2 NRs due to their large surface area. In addition, the mixed-phase TiO_2 nanostructures as photoanodes become remarkable materials for development due to their improved photovoltaic performance [5, 14, 41]. The deposition of anatase TiO_2 NPs by spray pyrolysis deposition and its paste by screen-printing method presents higher η than that of the pure phase (rutile) [5, 42]. In the present work, rutile TiO_2 NWs synthesised by hydrothermal growth method [39] and anatase TiO_2 NPs fabricated by squeegee method [43] were used as bottom and upper layers of photoanode layer, respectively. These methods were selected due to their low cost and simple fabrication. The novel combination of highly conductive hybrid CE thin-film-based TC14-rGO_MWCNTs with low Pt loading (10 nm) and rutile-anatase mixed-phase TiO_2 NWs/TiO_2 NPs resulted in improved DSSCs performance due to the enhanced photovoltaic performance.

2 Materials and methods

2.1 Fabrication of CE thin film

GO synthesis was carried out by electrochemical exfoliation method with customised triple-tail TC14 surfactant [13, 14]. Two graphite rods as starting materials were immersed in water-based electrolyte solution (0.1 M) and connected to 7 V DC power supply for 24 h exfoliation time. The excess oxygen functional groups in GO were chemically reduced by utilising hydrazine hydrate as reducing agent at 100:1 (GO:hydrazine hydrate). This reduction process was performed for 24 h at ~ 95 °C to produce rGO (TC14-rGO). Pristine MWCNTs and hybrid solution were prepared by dispersing 1 wt% MWCNTs into ethanol and TC14-rGO, respectively, and stirring for about 1 h to ensure that MWCNTs were well dispersed in the solution. The produced TC14-rGO, MWCNTs and TC14-rGO_MWCNTs solution were deposited onto preheated (120 °C) clean fluorine-doped tin oxide (FTO) substrates by spraying deposition method using an airbrush at 10 cm distance between the nozzle and the substrate. The film was annealed at 400 °C for 1 h in ambient argon. The thickness of fabricated pristine TC14-rGO was ~ 50 nm, while the pristine MWCNTs and TC14-rGO_MWCNTs hybrid presents thicker films of ~ 80 nm. The experimental designs of the TC14-rGO and TC14-rGO_MWCNTs hybrid thin film fabrication are presented in Fig. 1a. The clean FTO substrate and fabricated TC14-rGO and TC14-rGO_MWCNTs thin films were coated with 10 nm Pt NPs using coater sputter Quorum Q150R S. Hence, the TC14-rGO_MWCNTs/Pt and TC14-rGO/Pt films present ~ 90 and ~ 60 nm, respectively.

2.2 Fabrication of mixed-phase TiO_2 nanostructures

Mixed-phase TiO_2 nanostructures were synthesised by hydrothermal growth [39] and squeegee method [43], respectively; these nanostructures contained rutile TiO_2 NWs and anatase TiO_2 NPs at the bottom and upper photoanode layers, respectively. The hydrothermal solution was prepared from hydrochloric acid (HCl), DI water and titanium butoxide (TBOT) at 1:1:0.03 ratio. FTO substrates were placed at 45° against autoclave wall with the conducting surface facing downward before pouring the hydrothermal solution. The hydrothermal growth of rutile TiO_2 NWs was allowed at 150 °C for 20 h. The synthesised film was rinsed with DI water and dried at room temperature prior to annealing at 450 °C for 30 min. The TiO_2 NPs paste was prepared from titanium (IV) oxide, ethanol and titanium

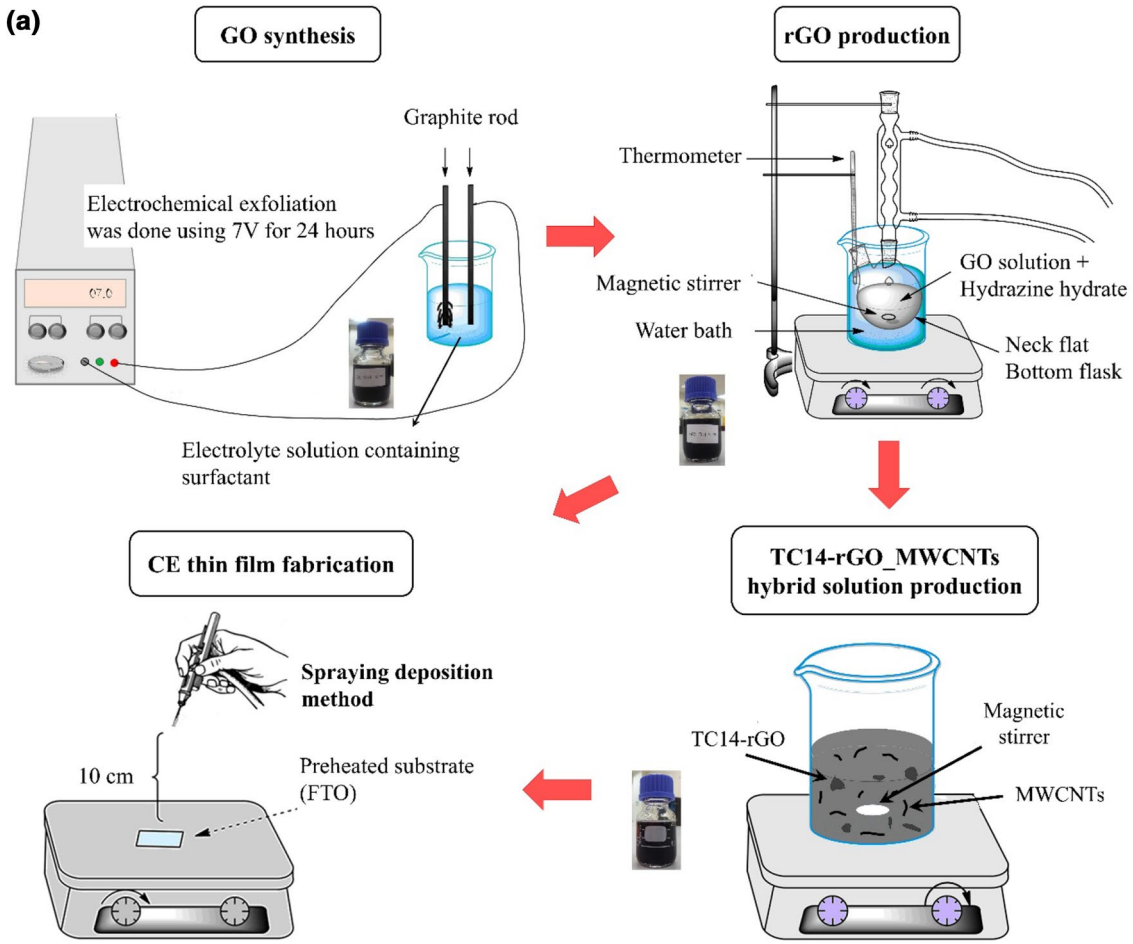

Fig. 1 Schematic diagram of **a** various reduced graphene oxide (rGO)-based counter electrode (CE) thin film fabrications, **b** hydrothermal growth method of TiO_2 nanowires (NWs) and squeegee method of TiO_2 NWs/TiO_2 nanoparticles (NPs) photoanode film and **c** dye-sensitised solar cells (DSSCs) fabrication

(IV) isopropoxide (TTIP) and sonicated for 5 min. The paste was well mixed to obtain little agglomeration. The obtained paste was applied on rutile TiO_2 NWs film using a glass rod by squeegee method. The films were heated at 150 °C for 10 min and annealed at 450 °C for 1 h. The experimental design of the mixed-phase TiO_2 nanostructure fabrication is displayed in Fig. 1b.

2.3 Fabrication of DSSCs

DSSCs fabrication was firstly performed by immersing mixed-phase TiO_2 nanostructures as photoanodes into N719 dye (0.3 mM) for 24 h. The dye solution was prepared by dissolving N719 powder into acetonitrile and 1-butanol (1:1, v/v). When the dyed photoanode was rinsed with ethanol to remove the residues and dried at room temperature, the photoanode and thin CE film were assembled, and an electrolyte was poured into the space between them. 1,2-Dimethyl-3-propylimidazolium iodide, which contains triiodide/iodide redox couple, was used as electrolyte. The assembled film was measured by solar simulator device. The experimental design of DSSCs fabrication is illustrated in Fig. 1c.

FESEM-Hitachi SU8020 and EDX-Horiba EMAX were used to investigate the morphologies and elemental compounds of fabricated photoanode and CE thin films. HRTEM-JEOL JEM 2100, XRD-Bruker D8 Advance and micro-Raman spectroscopy (Renishaw InVia Micro-Raman System) were utilised to investigate the structural properties. Diffrac.eva V4.0 software was used to determine the phase, crystallite size and crystallite percentage from XRD data. The integral (I) breath measurement was preferred rather than the full width at half maximum due to its accuracy. The film thickness determination was done by using Ellipsometer. The optical and electrical properties of fabricated film were measured by Agilent Technologies Cary 60 UV–Vis, four-point probe equipment with Keithley 2636A as sourcemeter and Leios TMXpert software as data analysis. Solar simulator Oriel Sol 1A under 1 M solar

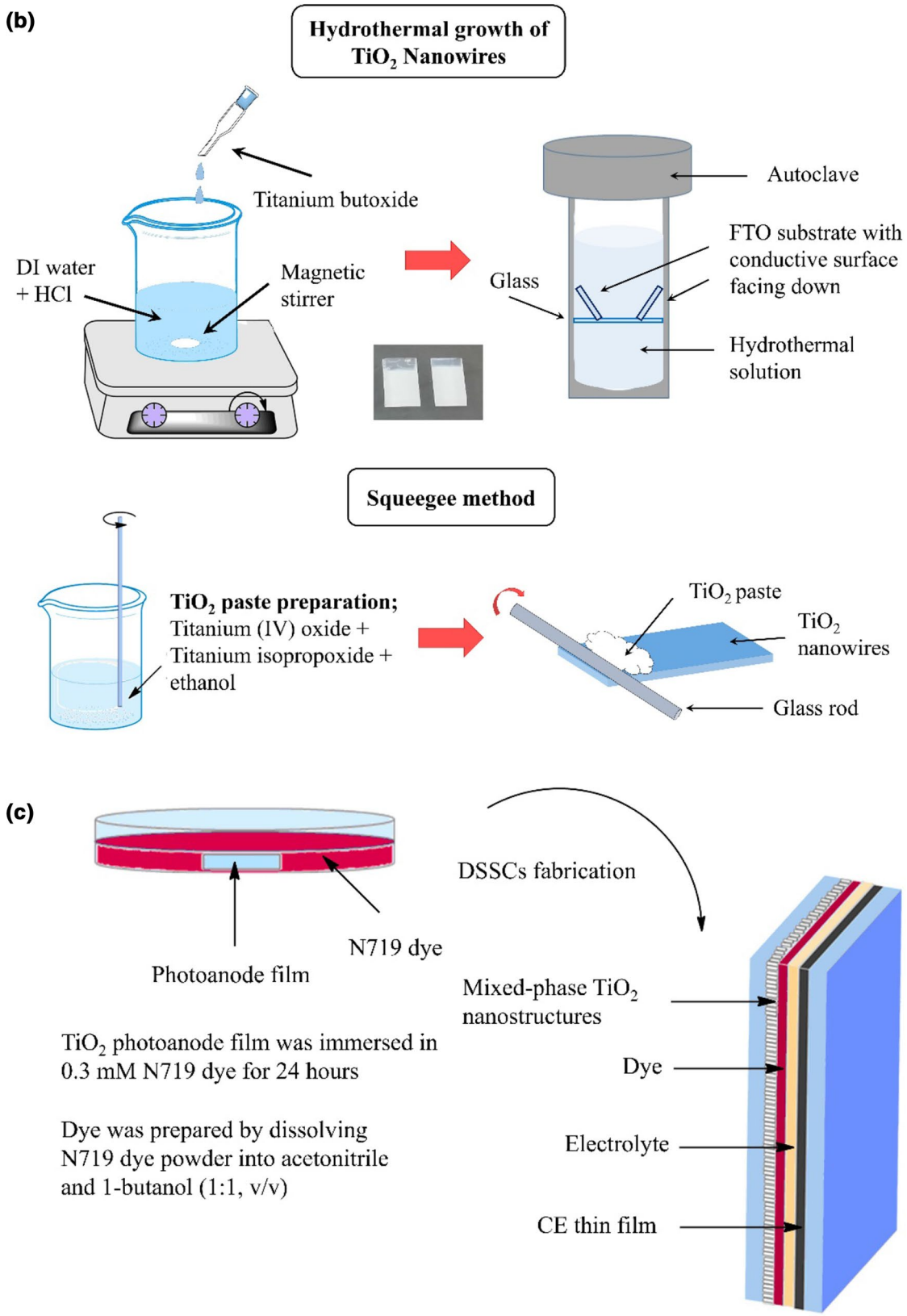

Fig. 1 (continued)

illumination was used for DSSCs efficiency measurement. In addition, EIS analysis (Potentiostat Galvanostat (Auto Lab), PGSTAT12/30/302) was also used to investigate the charge transfer resistance of fabricated DSSCs.

3 Results and discussion

3.1 FESEM, EDX and HRTEM analyses

The morphologies of fabricated TiO_2 NWs/TiO_2 NPs photoanode film determined by FESEM are shown in Fig. 2. Dense and uniform TiO_2 NWs were successfully grown on the entire FTO substrate without any crack (Fig. 2a). A close view shows that the synthesised TiO_2 NWs are consisted of tetragonal crystal structure with a diameter range of 47.6–226 nm (Fig. 2b). This tetragonal shape may be attributed to the abundant H^+ and Cl^- resulting from the decomposition of highly acidic HCl solution, which promotes the slow hydrolysis rate during the hydrothermal process and becomes an important factor in growing crystalline TiO_2 NWs [44, 45]. The precursor type used for the hydrothermal solution also affected the morphologies of produced TiO_2 NWs films. The use of TBOT offered medium hydrolysis rate compared with those of titanium tetrachloride ($TiCl_4$) and TTIP: $TiCl_4$ > TBOT > TTIP; this result supported the requirement of slow hydrolysis rate for TiO_2 NWs production. Moreover, TiO_2 NWs showed rough surface on the upper end of NWs, which provided an advantage for light scattering and electrolyte penetration. The rough surface increased the light scattering and trapping effect, thereby increasing the absorbed photon and exciting many electrons. A rough surface also suggests a highly hydrophilic surface, which increases the electrolyte penetration and consequently accelerates the dye regeneration [46]. The perpendicular direction of synthesised TiO_2 NWs to the FTO substrate was clearly observed on the cross-section view, with an average thickness of 3.29 μm (Fig. 2c). This result was attributed to the substrate positioning during hydrothermal growth; the vertical substrate position prevented the excess nucleating centres and promoted the perpendicular direction of TiO_2 NWs. The epitaxial growth of TiO_2 NWs was also supported by that TiO_2 and FTO display similar crystal structures [44].

The uniform and porous structure of TiO_2 NPs with particles closely adhering was evident when they were applied on TiO_2 NWs (Fig. 2d). The average TiO_2 NPs diameter was ~ 25 nm, which corresponded with that of titanium (IV) oxide particle size used as starting material for TiO_2 paste (Sigma Aldrich, 718467). This observation was in good agreement with that of previous study, which also utilised TiO_2 NPs as upper photoanode layer [5, 14, 43]. The TiO_2 NPs on TiO_2 NWs closely adhered without any gap, and they were not easily collapsed or peeled off due to the appropriate TTIP molar ratio (0.1 M) used in paste preparation (Fig. 2e). The total thickness of TiO_2 NWs/TiO_2 NPs was 15.6 μm, with approximately 23% thickness (3.62 μm) from TiO_2 NWs. TiO_2 NWs in TiO_2 NWs/TiO_2 NPs samples were thicker than those of pure TiO_2 NWs (3.29 μm), which may be due to the effects of annealing treatment on TiO_2 NWs after hydrothermal synthesis. During annealing, the Ti compound, which may still remain in the TiO_2 NWs sample even after rinsing process, was further grown; consequently, its thickness was 0.33 μm, which was 10% thicker than that of non-annealed TiO_2 NWs film. In this work, the thick TiO_2 NPs (~ 12 μm) with porous structure promoted the high amount of dye adsorption, which increased the number of excited electrons. Further EDX analysis confirmed titanium (Ti) and O (oxygen) as elemental compounds of pure TiO_2 NWs and TiO_2 NWs/TiO_2 NPs photoanode film. The higher Ti atomic percentage of TiO_2 NWs/TiO_2 NPs sample (28.83%) than that of pure TiO_2 NWs (28.30%) was due to the addition of TiO_2 NPs. The O atomic percentages of pure TiO_2 NWs and TiO_2 NWs/TiO_2 NPs photoanode film were 71.70 and 71.17%, respectively, as shown in Fig. 2f and g, respectively.

The FESEM images of various CE thin films (TC14-rGO, MWCNTs, TC14-rGO_MWCNTs hybrid, TC14-rGO/Pt and TC14-rGO_MWCNTs/Pt) are presented in Fig. 3. The thin layer of TC14-rGO is evidently stacked on FTO substrate, as shown by the yellow arrow (Fig. 3a). The utilisation of triple-tail surfactant resulted in highly wrinkled and crumpled-tissue-like morphology on the rGO basal plane with less agglomeration. This was believed due to the role of surfactant tail number, which the triple-tail TC14 surfactant promoted triple higher interactions between the tail surfactant number and the graphite layers thus efficiently oxidized and exfoliated the graphite layer during GO synthesis as compared to the commercial single- or double-tail surfactant. This observation also confirmed the efficiency of TC14 surfactant in promoting the rGO layer stabilisation, where the wrinkled structure prevented the layer from restacking. The successful oxidation during exfoliation process was supported by the fold-up rGO layers, which are shown in red arrows. The transparent layer is shown with bright colour in the edge part of rGO layer (pointed by blue arrow), which may be due to the resultant defect after reduction process and the isolated oxygen reaction sites; this layer also confirmed the thin layer of produced rGO [13, 32]. Such result was also verified with the HRTEM images showing fold-up layers on the edge plane (Fig. 3b). The thin layer of TC14-rGO was in good agreement with that of previous work, which shows ~ 2–4 layers of produced TC14-rGO [14]. With regard to the pristine Pt CE thin film, Pt NPs evenly covered the entire FTO substrate without eliminating the FTO grain boundaries due to the thin Pt coating of only 10 nm (Fig. 3c). This observation was further confirmed by

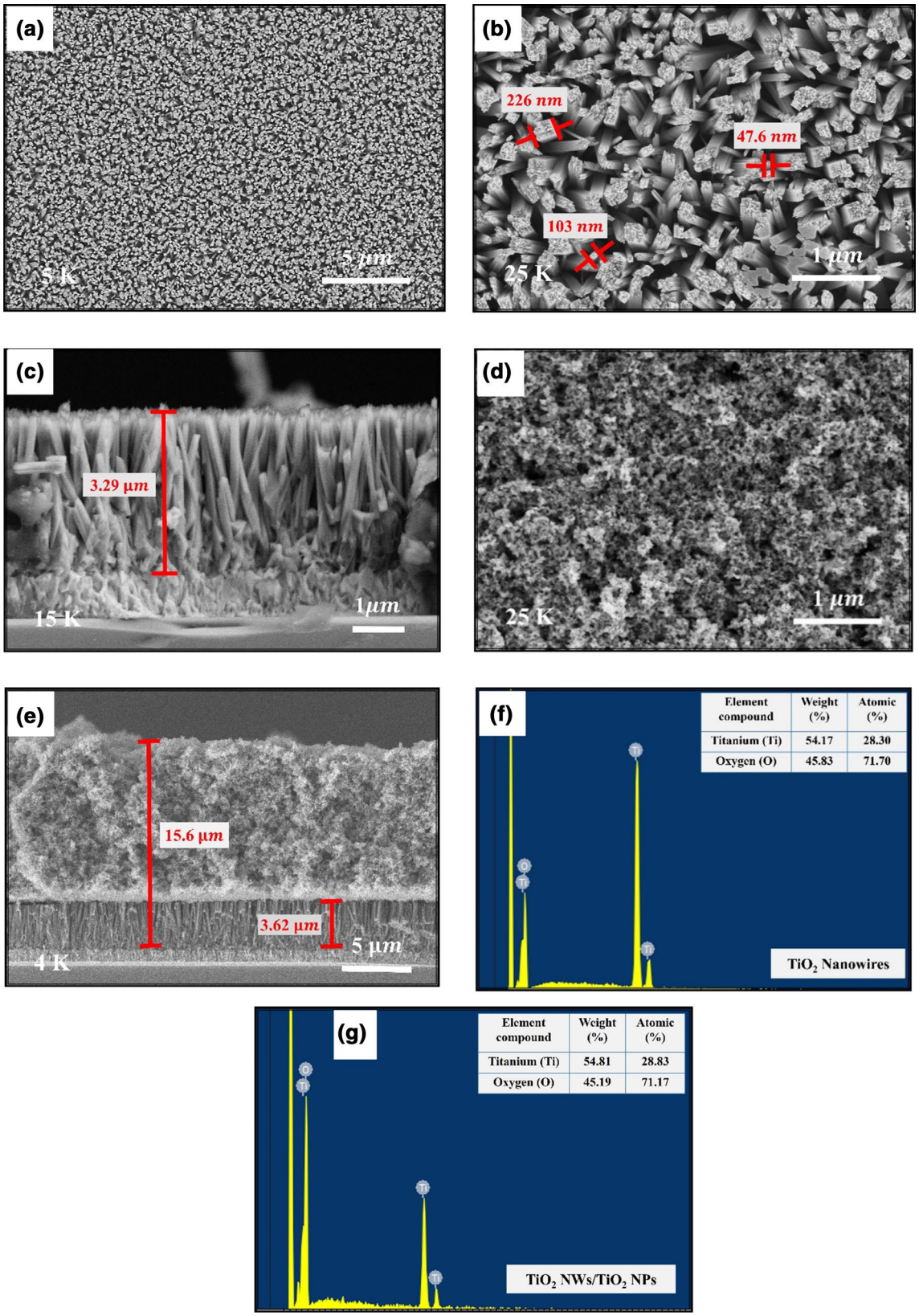

Fig. 2 FESEM images of the **a** top view, **b** diameter range and **c** cross section of TiO_2 NWs, **d** top view of TiO_2 NPs, and **e** cross section of TiO_2 NWs/TiO_2 NPs. EDX analysis result for **f** TiO_2 NWs and **g** TiO_2 NWs/TiO_2 NPs

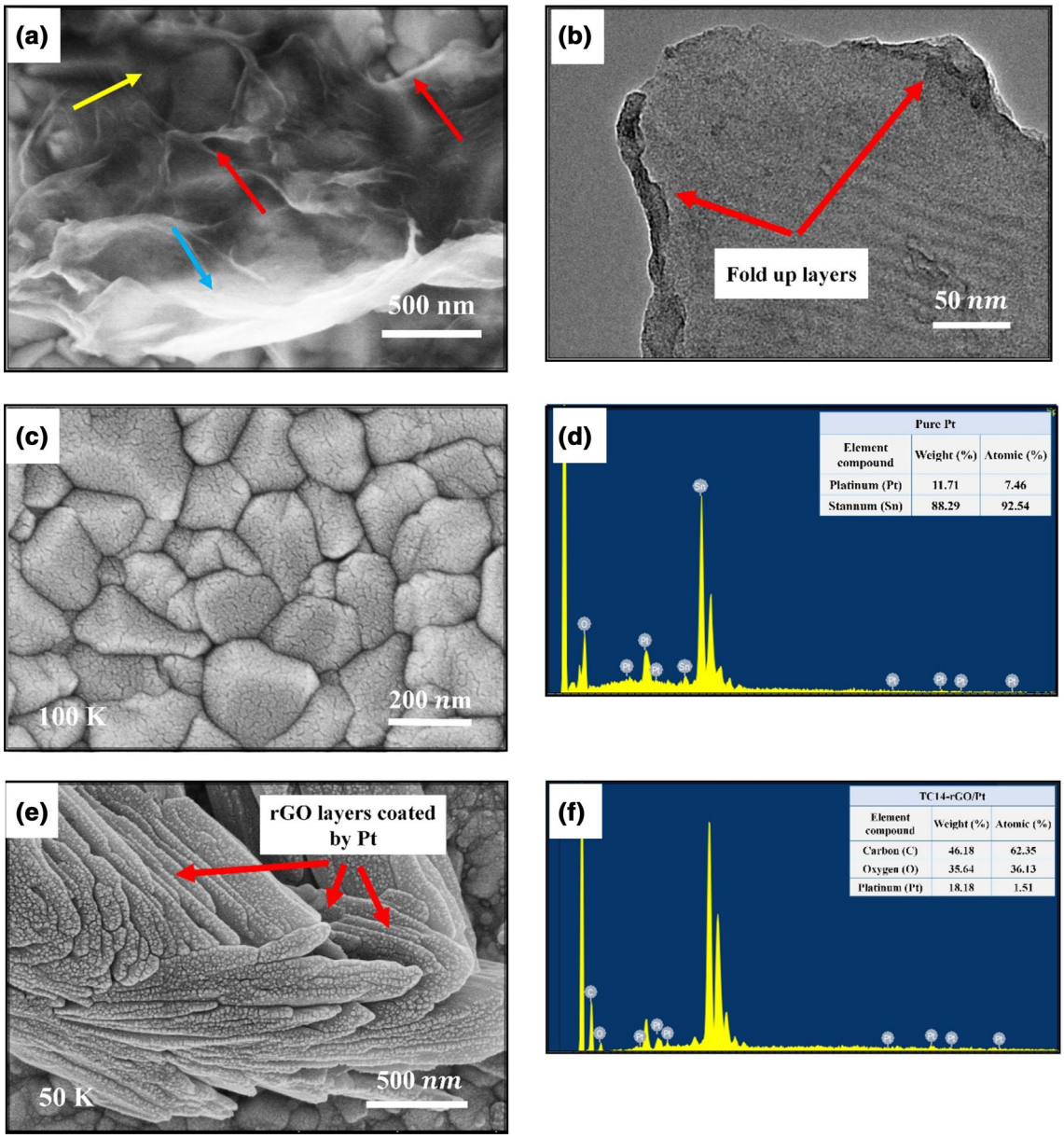

Fig. 3 **a, b** FESEM and HRTEM images of TC14-rGO; FESEM images and EDX analysis of **c, d** Pt NPs and **e, f** TC14-rGO; **g** diameter of Pt NPs; **h** FESEM images of MWCNTs; and FESEM and EDX analysis of **i, j** TC14-rGO_MWCNTs and **k, l** TC14-rGO_MWCNTs/Pt CE thin film. (Color figure online)

high stannum (Sn) atomic percentage (92.54%) as the FTO substrate compound over the Pt atomic percentage (7.46%) analysed by EDX (Fig. 3d).

The thin-layer TC14-rGO (Fig. 3a) became thick when it was coated with Pt NPs, as shown in Fig. 3e. Pt NPs uniformly covered the entire TC14-rGO layers, as shown by the red arrows. A close view shows that Pt NPs closely adhered to the TC14-rGO layers and formed a small cluster, with an average diameter of 4.96–8.93 nm (Fig. 3g). This value was in good agreement with the result obtained by Fang et al. [47]. The small size of Pt NPs and the cluster yielded a better performance than that of large size particle (> 10 nm) [20]. EDX analysis revealed the higher carbon (C) atomic percentage (62.35%) than that of O (36.13%). This result also confirmed the successful reduction process by hydrazine hydrate to reduce oxygen functional groups from TC14-GO solution (81.98% of O content [14]), as performed in previous study, and characterised a rGO. Low Pt atomic percentage (1.51%) further verified the thin Pt coating (only 10 nm) of TC14-rGO/Pt sample (Fig. 3f).

Pristine MWCNTs from WCPO thin film showed bundles formed from many individual MWCNTs. The diameter of

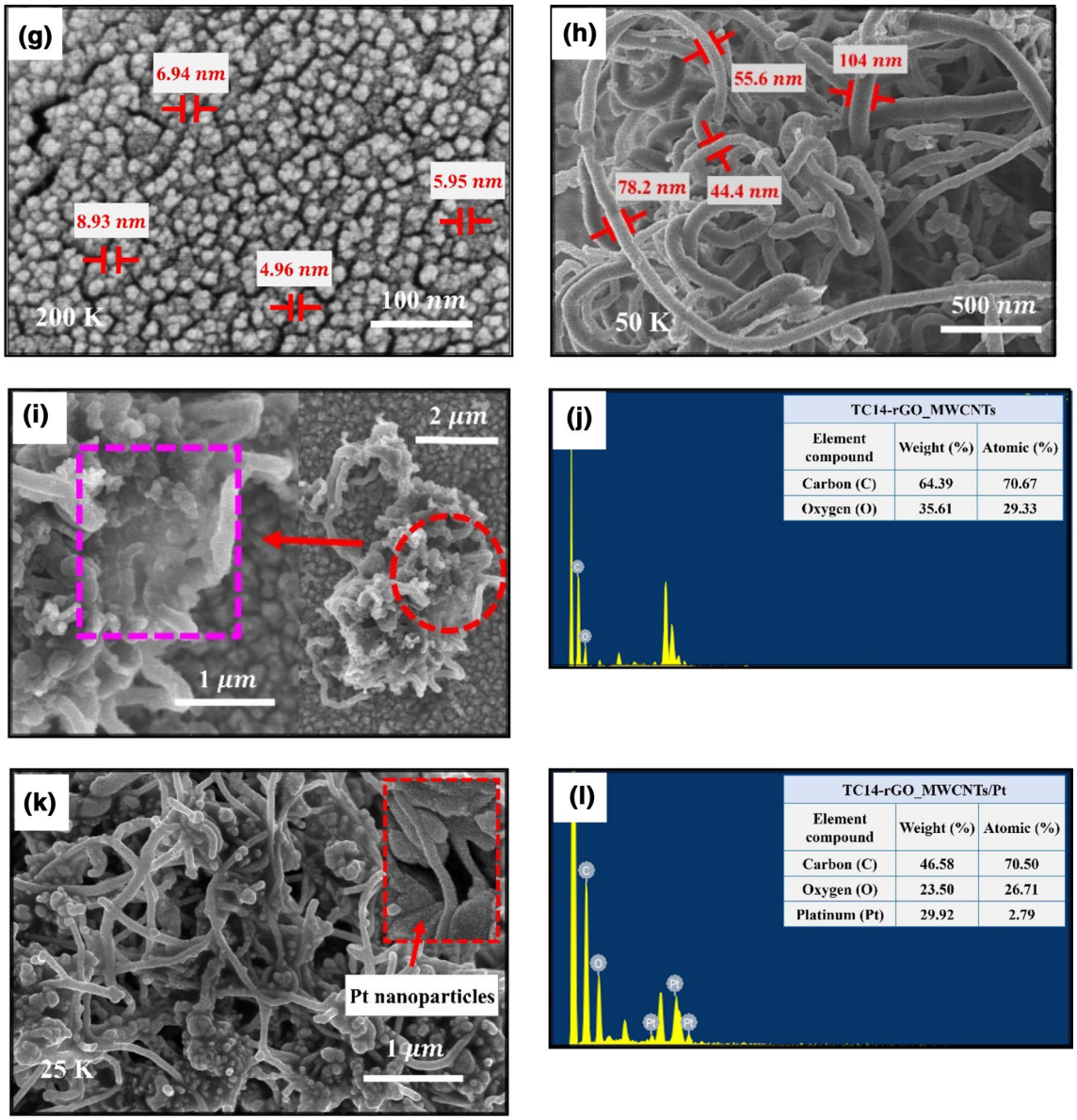

Fig. 3 (continued)

these MWCNTs was in the range of 44.4–104 nm (Fig. 3h). When MWCNTs were hybridised with TC14-rGO, small bundles of MWCNTs cluster were observed strongly stacked on TC14-rGO layer, which provided high surface area for TC14-rGO_MWCNTs film [48]. TC14-rGO acted as a binder and bound each individual MWCNTs. The empty are in pristine MWCNTs sample shown in Fig. 3h was filled with TC14-rGO, as shown by the purple rectangle in Fig. 3i. MWCNTs also prevent the TC14-rGO layer aggregation by occupying the internal spacing of rGO layers [49]. According to the EDX analysis, the higher C atomic percentage of TC14-rGO_MWCNTs (70.67%) than that of pristine TC14-rGO (66.66% in previous result [14]) was caused by the high C content of MWCNTs (Fig. 3j).

When Pt NPs were used to coat the TC14-rGO_MWCNTs hybrid film, it covered the entire film, as shown in Fig. 3k. Pt coating was performed to increase the catalytic surface area and the photocatalytic activity of the film. A higher C atomic percentage (70.50%) than that of O (26.71%), a rGO characteristic (Fig. 3l), was also observed. This value was similar to that of TC14-rGO_MWCNTs film.

3.2 Micro-Raman spectroscopy

The micro-Raman spectra of TiO_2 NWs are shown in Fig. 4. The synthesised TiO_2 NWs were in rutile phase, as confirmed by three Raman active modes of rutile; these modes are expressed as $A_{1g}+B_{1g}+E_g$ from the observed peaks at

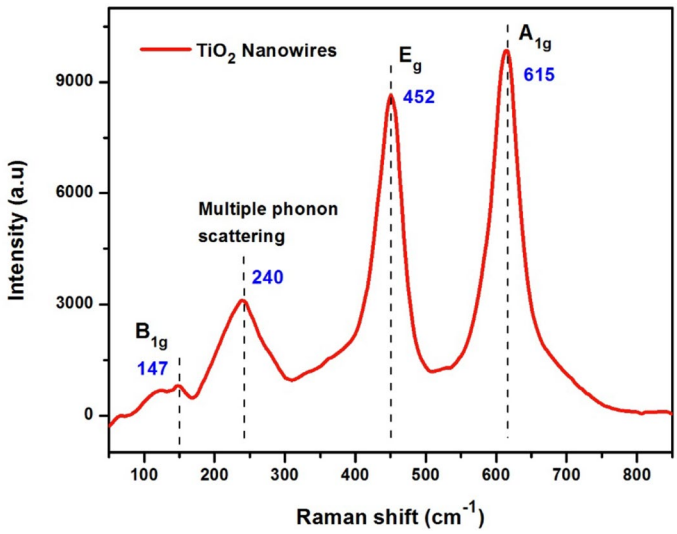

Fig. 4 Micro-Raman spectra of rutile TiO_2 NWs

615, 147 and 452 cm^{-1}, respectively [37, 50–53]. The A_{1g} and B_{1g} modes are caused by the antisymmetric and symmetric bending vibrations of O–Ti–O, respectively; E_g is attributed to the O–Ti–O symmetric stretching vibration in TiO_2 [54]. The multiple phonon scattering due to the disordered lattice occurred at 240 cm^{-1}, which indicated the nanometer scale of TiO_2 NWs; these results also confirmed the observation in FESEM images [37].

The micro-Raman spectra of TC14-rGO, Pt and TC14-rGO/Pt CE thin films are presented in Fig. 5a. The TC14-rGO spectra showed the D-, G-, G^+- and 2D-band peaks at 1356, 1586, 1622 and 2718 cm^{-1} respectively. D-band occurred due to the internal structural defects caused by vibration of C atoms with dangling bonds, which suggested the amount of defects or disorder in the sample. This band was also attributed to the sp^3 hybridisation of C, which was

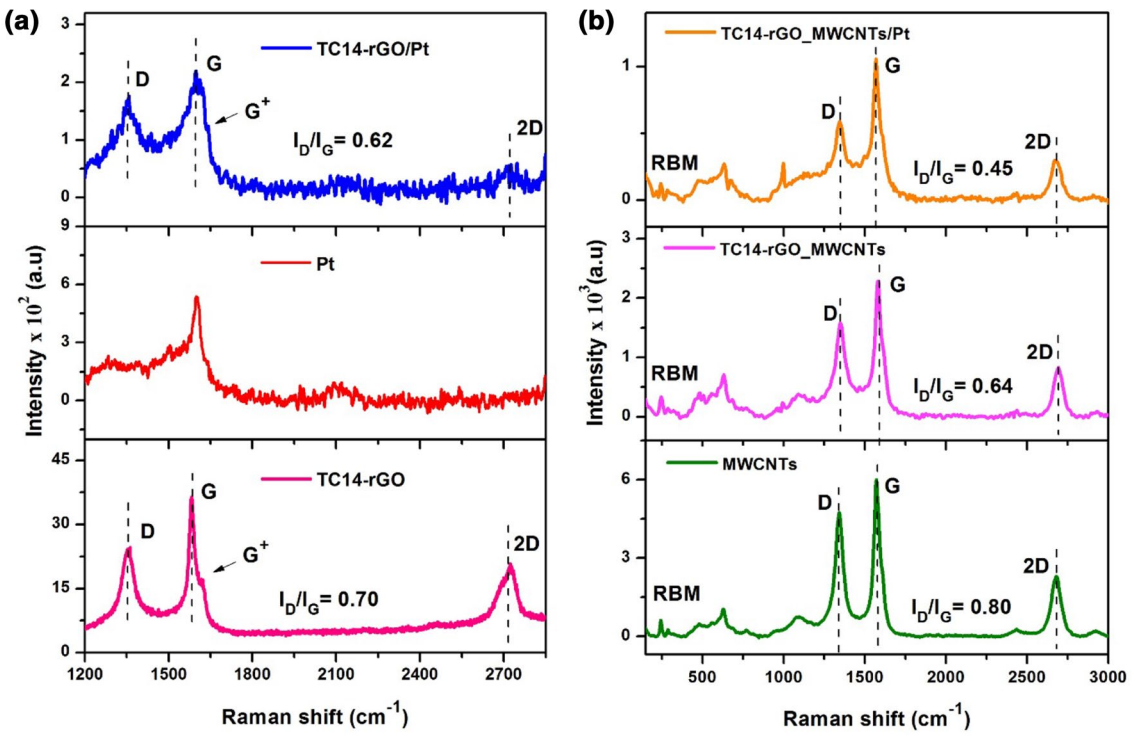

Fig. 5 Micro-Raman spectra of **a** pristine TC14-rGO, Pt and TC14-rGO/Pt and **b** pristine MWCNTs and their hybridised (TC14-rGO_MWCNTs and TC14-rGO_MWCNTs/Pt) CE thin films

related to A_{1g} mode symmetry [40, 55, 56]. The G-band resulted from the vibration of sp^2-bonded C atoms and corresponded to E_{2g} mode. This peak also characterises a C material, and it can be used to estimate the rGO layer number [57]. According to the equation $\omega_G = 1581.6 + 11/(1 + n^{1.6})$ [58], where ω_G is the G-band position, the layer number of TC14-rGO was 1.95; this value confirmed the thin rGO layer and proved the HRTEM images of previous work (~2–4 layers) [14]. The observed peak at 1622 cm^{-1}, which represented the G^+-band, indicated high disorder or defect level (both on the basal and edge planes of rGO layer); this defect was the crumpled-tissue-like structure of the film illustrated in FESEM images. Such defect is due to the intravalley double resonance process, and it confirmed that the intercalation process is promoted by triple-tail TC14 surfactant during oxidation and the hydrazine hydrate during reduction [57]. The last peak at 2718 cm^{-1} (2D-band) can also be used to estimate the layer number of rGO. According to the spectrum, the observed high and sharp peak confirmed the thin rGO layer demonstrated by FESEM and HRTEM images (Fig. 3a, b). The shifted peaks of TC14-rGO (1356, 1586, 1622 and 2718 cm^{-1}) observed in this work compared with those of previous work [14] on TC14-GO (1355, 1585, 1619 and 2714 cm^{-1}) showed the successful reduction process.

When TC14-rGO was coated with Pt, all peaks were red shifted to 1373, 1595, 1639 and 2719 cm^{-1} for D-, G-, G^+- and 2D-bands, respectively. The G^+-band was still evident in TC14-rGO/Pt even after Pt coating, which confirmed the high-level defect on the sample. The defect level of the sample can be determined by calculating the intensity ratio of D- to G-band peak (I_D/I_G). The calculated I_D/I_G ratio of TC14-rGO/Pt film showed a value (0.62) lower than that of pristine TC14-rGO (0.70). The difference may be due to the Pt coating, which adhered closely to TC14-rGO layer, thereby affecting the spectrum. Overall, TC14-rGO and TC14-rGO/Pt showed high I_D/I_G value, which indicated high-level defect after the reduction process on TC14-GO [59]. This result also verified the effectiveness of hydrazine hydrate in removing some parts of oxygen functional groups, which was also supported by the high C atomic percentage shown in EDX analysis (Fig. 3f) [60, 61].

The micro-Raman spectra of pristine WCPO-based MWCNTs and its hybridisation with TC14-rGO and Pt NPs are displayed in Fig. 5b. Overall, the MWCNTs-based CE thin films presented the same A_{1g} symmetry radial breathing mode (RBM) as the main characteristic of SWCNTs observed in the low frequency of ~242.3 cm^{-1} [49, 62]. The detected RBM peaks confirmed the low (< 2 nm) intertube diameter of synthesised CNTs [28]. Moreover, a peak observed at ~629 cm^{-1} is due to the intense laser irradiance [62]. The I_D/I_G ratio was used to investigate the CNTs graphitisation degree, which was high (0.80); this value indicated low graphitisation and confirmed the multiwalled CNTs synthesised from WCPO [63, 64]. The pristine MWCNTs showed a sharp D-, G- and 2D-band peaks at 1342, 1575 and 2679 cm^{-1}, respectively. When MWCNTs were hybridised with TC14-rGO, the D-, G- and 2D-band peaks were red shifted to 1352, 1583 and 2692 cm^{-1}, respectively. This result indicated that the interactions between MWCNTs intertubes decreased due to the physical constraints caused by the addition of TC14-rGO between the individual MWCNTs [65]. The I_D/I_G ratio of TC14-rGO_MWCNTs exhibited a lower value (0.64) than that of pristine MWCNTs film. The difference was due to the gradual incorporation of ideal sp^2 MWCNTs structure into high-defect rGO [66]. Furthermore, the D- and G-band peak widths were slightly wide (91 and 57 cm^{-1}) due to the disorder between TC14-rGO hexagonal structure and MWCNTs [67]. The D-band peak width became narrow (48 cm^{-1}) when the TC14-rGO_MWCNTs film was coated with Pt NPs. The I_D/I_G ratio of TC14-rGO_MWCNTs/Pt was also decreased to approximately 0.45 due to the Pt coating. This result was also consistent with that of TC14-rGO/Pt sample, which presented lower I_D/I_G ratio than that of pristine TC14-rGO. The D-, G- and 2D-band peaks of TC14-rGO_MWCNTs/Pt were blue shifted to 1347, 1573 and 2679 cm^{-1}, respectively. The summary of the micro-Raman peaks of CE thin films is presented in Table 1.

3.3 XRD analysis

The XRD patterns of synthesised TiO_2 NWs and fabricated TiO_2 NWs/TiO_2 NPs photoanode films are shown in Fig. 6. Figure 6a illustrates that the synthesised TiO_2 NWs film was

Table 1 Micro-Raman peak summary of fabricated CE thin films

No.	CE thin films	D-band (cm^{-1})		G-band (cm^{-1})		G^+-peak (cm^{-1})	2D-band (cm^{-1})		I_D/I_G
		Peak	Width	Peak	Width		Peak	Width	
a	TC14-rGO	1356	75	1586	52	1622	2718	60	0.70
b	TC14-rGO/Pt	1373	198	1595	81	1639	2719	56	0.62
c	MWCNTs	1342	63	1575	51	-	2679	58	0.80
d	TC14-rGO_MWCNTs	1352	91	1583	57	-	2692	60	0.64
e	TC14-rGO_MWCNTs/Pt	1347	48	1573	58	-	2679	57	0.45

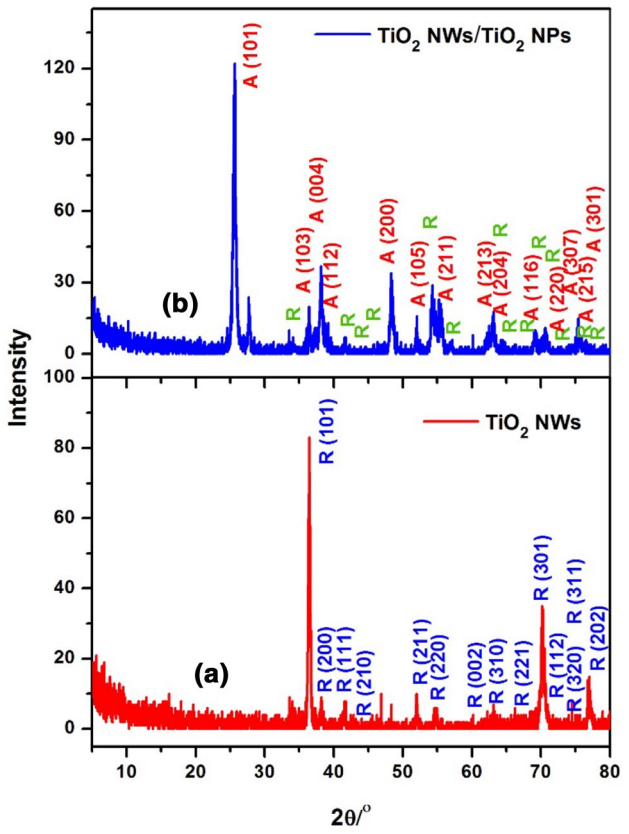

Fig. 6 XRD patterns of **a** pure TiO_2 NWs and **b** TiO_2 NWs/TiO_2 NPs photoanode films

in the rutile phase. A total of 14 peaks were observed in the range of 5°−80°, with the most intense peak representing plane [101] at 36.49° (PDF No.01-071-4809). Two more intense peaks were observed at 70.04° and 77.54°, which represented planes [301] and [202], respectively. Crystallinity measurement revealed that TiO_2 NWs possessed high crystallinity (89%), as confirmed by the high and sharp XRD pattern shown in Fig. 6a. Additionally, the crystallite size measured by I breadth (Table 2) showed the average size of 21.9–56.4 nm, which was larger than that of TiO_2 NRs (the largest crystallite size is 31 nm) [14]. Large crystallite size resulted in improved electrical performance and better photovoltaic performance of TiO_2 NWs than that of TiO_2 NRs. In addition, the high crystallite percentage of TiO_2 NWs film (89%), with four selected peaks presenting considerably high crystallinity percentage of approximately 97.4%, confirmed the good quality of synthesised film. This high crystallite percentage of TiO_2 NWs was also higher than that of TiO_2 NRs [14]. Large crystallite size and high percentage suggested the better performance of TiO_2 NWs than that of TiO_2 NRs for DSSCs application.

Fourteen additional peaks, which represented the anatase phase of TiO_2 NPs (PDF No.01-075-1537), were observed

Table 2 Crystallite sizes and percentages of selected peaks of (a) pure TiO_2 NWs and (b) TiO_2 NWs/TiO_2 NPs photoanode films (A: anatase, R: rutile)

No.	TiO_2 films	Peak (°)	Crystallite size (nm)	Crystallite percentage (%)
a	TiO_2 NWs	35.5–37.5	27.7	95.1
		41–42	56.4	97.4
		69–71.5	21.9	87.3
		76–78	32.4	95.5
b	TiO_2 NWs/TiO_2 NPs	24.5–27 (A)	18.9	87.3
		37–39 (A–R)	25.9	70.2
		47–50 (A)	19.5	89.9
		69–71.5 (A–R)	48.8	94.8
		76–78 (A–R)	70.3	89.6

when these NPs were applied on TiO_2 NWs as the second layer of photoanode film (Fig. 6b). The plane [101] located at 25.65° presented the most intense peak, which also became a characteristic of anatase phase. Two other intense and sharp anatase peaks were observed at 38.39° and 48.79°. The thick TiO_2 NPs completely covered the TiO_2 NWs with good attachment, which was confirmed by the low rutile intensity peak originally located at 36.49° and 70.04°. Furthermore, the anatase crystallite sizes of TiO_2 NWs/TiO_2 NPs at 25.65° and 48.79° were accurately the same as those presented for TiO_2 NRs-NFs/TiO_2 NPs [14]. This result verified the consistent TiO_2 material and squeegee method in the fabrication of photoanode layer. The lower crystallite percentage of TiO_2 NWs/TiO_2 NPs photoanode film (82.5%) than that of pure TiO_2 NWs (97.4%) may be due to the porous TiO_2 NPs (Fig. 2d), which was confirmed by the ratio between rutile and anatase phases of 17.6 and 82.4%, respectively. This high crystallite percentage suggested the high dye adsorption by TiO_2 NPs, thereby making them applicable in photoanode film for DSSCs application.

3.4 Current–voltage (*IV*) measurement

The CE thin film resistivity values determined by four-point probes are presented in Fig. 7. The lowest resistivity was achieved by Pt (0.37 Ωcm). This result was due to the high conductivity of Pt and its being the thinnest one among CE thin films. By contrast, pristine TC14-rGO film exhibited the highest resistivity of 3.13 Ωcm. MWCNTs, as highly conductive materials, presented a slightly lower resistivity (3.12 Ωcm) than that of TC14-rGO. When both materials were hybridised (TC14-rGO_MWCNTs), the resistivity decreased to about 2.86 Ωcm due to the incorporation of highly conductive MWCNTs. The resistivity was further decreased to 2.48 and 2.29 Ωcm when Pt was coated on top

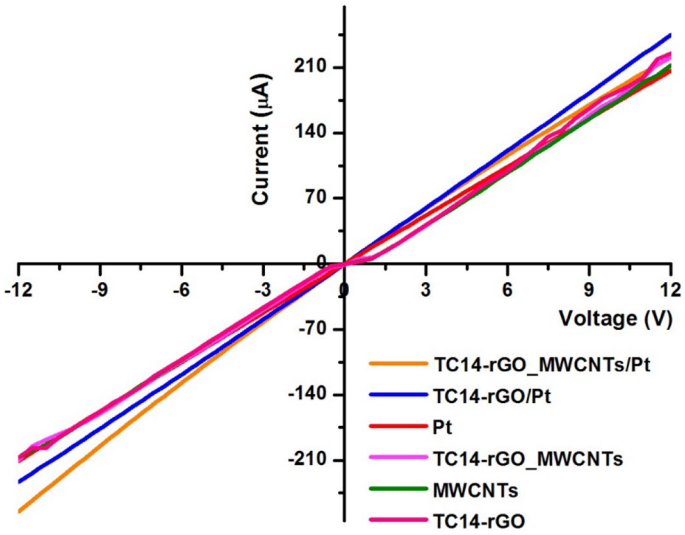

Fig. 7 Resistivity measurements of various CE thin films by using four-point probes. (Color figure online)

Table 3 Resistivity values of various CE thin films

CE thin films	Resistivity (Ωcm)
TC14-rGO_MWCNTs/Pt	2.29
TC14-rGO/Pt	2.48
Pt	0.37
TC14-rGO_MWCNTs	2.86
MWCNTs	3.12
TC14-rGO	3.13

of TC14-rGO and TC14-rGO_MWCNTs films, respectively, due to the high conductivity of Pt [68]. According to Fig. 7, the TC14-rGO/Pt graph was above the TC14-rGO_MWCNTs/Pt graph. This result was attributed to different film thicknesses, which affected the resistivity value. The resistivity values of various CE thin films are summarised in Table 3.

3.5 UV–Vis spectrophotometer

The transmittance values of pure TiO_2 NW**s**, TiO_2 NWs/TiO_2 NPs photoanode films and various CE thin films are presented in Fig. 8a. Both TiO_2 films displayed considerably low transmittance of 2.60 and 0.60% for pure TiO_2 NW**s** and TiO_2 NWs/TiO_2 NPs photoanode films, respectively. The low transmittance percentage of pure TiO_2 NW**s** was due to the dense as-grown film with small diameter, as shown in FESEM images. The transmittance was further decreased when TiO_2 NWs were coated with TiO_2 NPs due to the thick yet homogeneous and highly interconnected TiO_2 NPs. On the contrary, various fabricated CE thin films presented high transmittance of more than 90% for the CE without Pt coating film; the values were 92.81, 90.67 and 90.08% for TC14-rGO, MWCNTs and TC14-rGO_MWCNTs films, respectively. The low transmittance percentage of MWCNTs was probably due to the dense and bundle structures observed in FESEM images. When MWCNTs were hybridised with TC14-rGO, the transmittance was further decreased due to the highly stacked film. The bundled MWCNTs hindered the light movement and caused a decrease on the transmittance value. Notably, when TC14-rGO (TC14-rGO/Pt) was coated with Pt NPs, the transmittance value increased to approximately 40.63% compared with that of pristine Pt (35.13%). This result indicated that the TC14-rGO/Pt surface morphology favours the harvest of incident light [69]. Additionally, the low transmittance percentage of TC14-rGO_MWCNTs/Pt film (34.31%) can be due to the bundled form of MWCNTs.

Furthermore, the optical band gap energy (E_g) based on Tauc's plot exhibits lower value of TiO_2 NW**s**/TiO_2 NPs (2.93 eV) than that of the pure TiO_2 NWs (3.04 eV) (Fig. 8 b). The E_g value of TiO_2 NWs is in good agreement with that of pure rutile phase TiO_2 [70]. The low E_g value of TiO_2 NW**s**/TiO_2 NPs suggested the improved electron transport through the film, which became an advantage for DSSCs application. Fast electron transport through the device resulted in high η due to the high photovoltaic performance. Lower E_g value was observed in MWCNTs (4.06 eV) than that in TC14-rGO (4.07 eV), as shown in Fig. 8c. The difference was due to the high conductivity of MWCNTs materials. However, this result confirmed the good quality of produced rGO assisted by triple-tail surfactant, which showed the comparable E_g value with highly conductive MWCNTs. When TC14-rGO was hybridised with MWCNTs, the E_g value was decreased to 4.04 eV (Fig. 8d). This decrease indicated an improved electron movement through the film due to the low resistivity of hybridised film. When TC14-rGO and

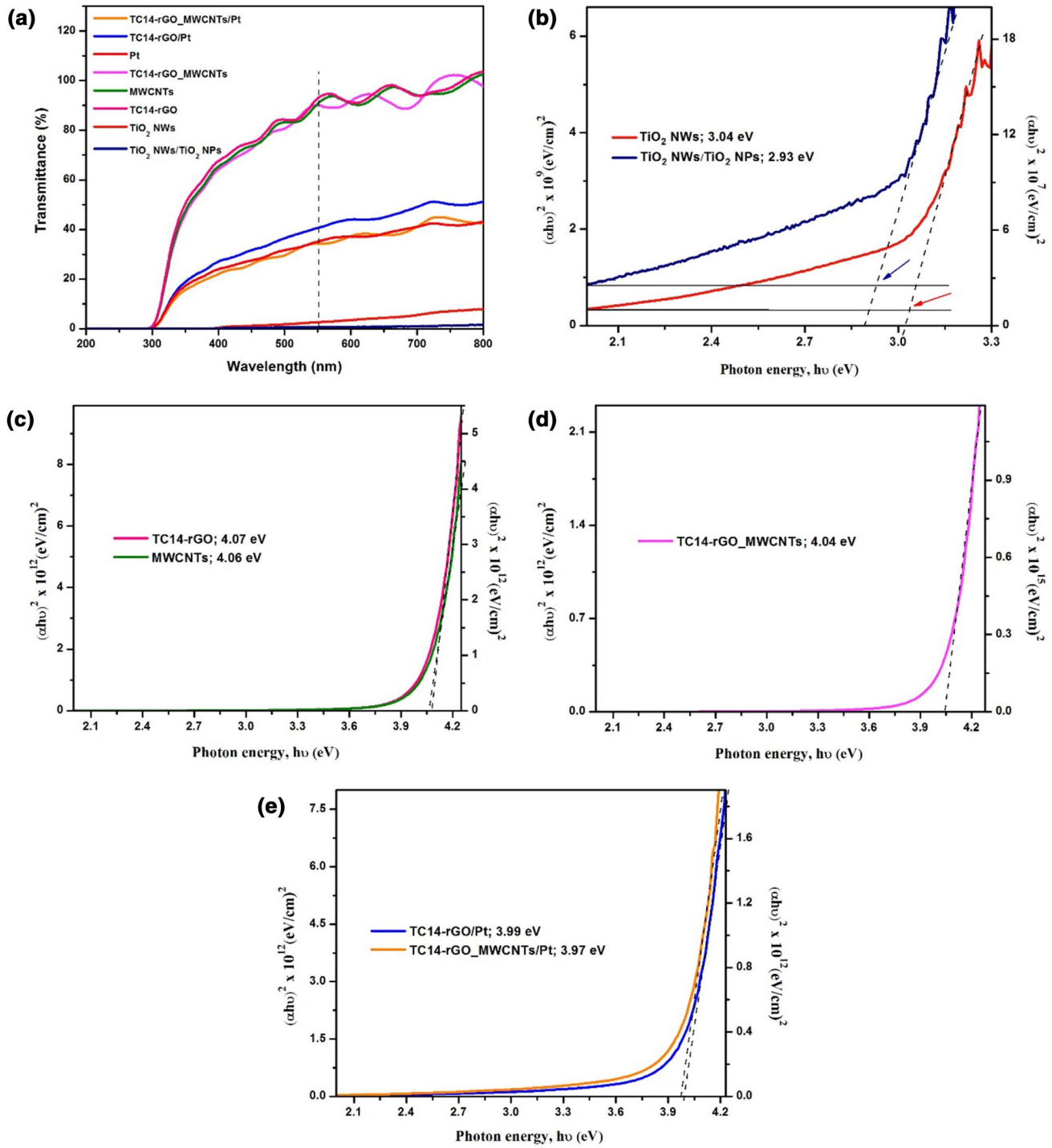

Fig. 8 **a** Transmittance values of pure TiO_2 NWs, TiO_2 NWs/TiO_2 NPs photoanode films and various CE thin films and **b–d** optical band gap energies (E_g) of photoanodes and CE thin films. (Color figure online)

TC14-rGO_MWCNTs hybrid films were coated with Pt, the E_g value was decreased further to 3.99 and 3.97 eV, respectively (Fig. 8e). This result demonstrated that the most remarkable optical properties of CE thin films were achieved by compositing TC14-rGO, MWCNTs and Pt.

Table 4 Transmittance and E_g values of various CE thin films

Photoanode and CE thin films	Transmittance (%)	Band gap energy (E_g, eV)
TiO_2 NWs	2.60	3.04
TiO_2 NWs/TiO_2 NPs	0.60	2.93
TC14-rGO_MWCNTs/Pt	34.31	3.97
TC14-rGO/Pt	40.63	3.99
Pt	35.13	-
TC14-rGO_MWCNTs	90.08	4.04
MWCNTs	90.67	4.06
TC14-rGO	92.81	4.07

The transmittance and E_g values of CE thin films are summarised in Table 4.

3.6 Solar simulator measurement

The solar simulator measurements of fabricated DSSCs are plotted as J_{SC}–V curves and presented in Fig. 9. CE based on pristine TC14-rGO and MWCNTs showed the same η of 0.017%. The similarity was probably due to the similar E_g (4.06 and 4.07 eV) and resistivity (3.12 and 3.13 Ωcm), which affected the electron transport through the film. This result further confirmed the good performance of rGO film assisted by triple-tail TC14 surfactant, which was proven by the same η even when compared with highly conductive MWCNTs material. This result was also supported by the higher V_{OC} (0.687 V) and J_{SC} (0.214 mA/cm^2) values of TC14-rGO than those of MWCNTs CE film, which were 0.441 V and 0.201 mA/cm^2, respectively. The wrinkled layer of TC14-rGO offers highly active area for electrolyte diffusion [13, 14, 71], thereby yielding higher V_{OC} and J_{SC} than those of cylindrical MWCNTs. In addition, the agglomerated MWCNTs, as observed on FESEM images, reduce the active area [48, 72]. Lower FF value of TC14-rGO (9.8) than that of MWCNTs (16.4) may be due to the lower roughness factor of the sheet-shaped TC14-rGO than that of the agglomerated MWCNTs [73]. High diffusion resistance due to the low electrical conduction from the isolated aromatic domains on TC14-rGO basal plane also decreased the FF value.

When both materials were hybridised (TC14-rGO_MWCNTs), η was increased 94–0.033%. The hybridised materials presented higher V_{OC} (0.752 V) and J_{SC} (0.330 mA/cm^2) due to their larger surface areas and active sites than that of pristine TC14-rGO or MWCNTs. This result was attributed to the suppression of strong π–π interaction by the hybrid material, which increases the electrocatalytic properties [48]. The loose structure of MWCNTs in TC14-rGO_MWCNTs structure decreases the internal resistance and consequently enhances the electron transport through the film [72]. This result was also supported by the lower E_g (4.04 eV) and resistivity (2.86 Ωcm) values of the hybridised materials than those of pristine TC14-rGO and MWCNTs. The conventional Pt CE film displayed a high η (1.445%) with V_{OC}, J_{SC} and FF values of 0.758 V, 3.974 mA/cm^2 and 38.8, respectively, due to the high electrical conductivity of material (the lowest resistivity of 0.37 Ωcm). This observation was verified by the small particle size and thin layer of Pt film, which further increase the electrocatalytically active surface area and result in fast electrolyte reduction [46].

Given the high η achieved by Pt NPs, further measurement was conducted by coating TC14-rGO and TC14-rGO_MWCNTs with these NPs. High η values were achieved for both coated films; TC14-rGO_MWCNTs/Pt presented

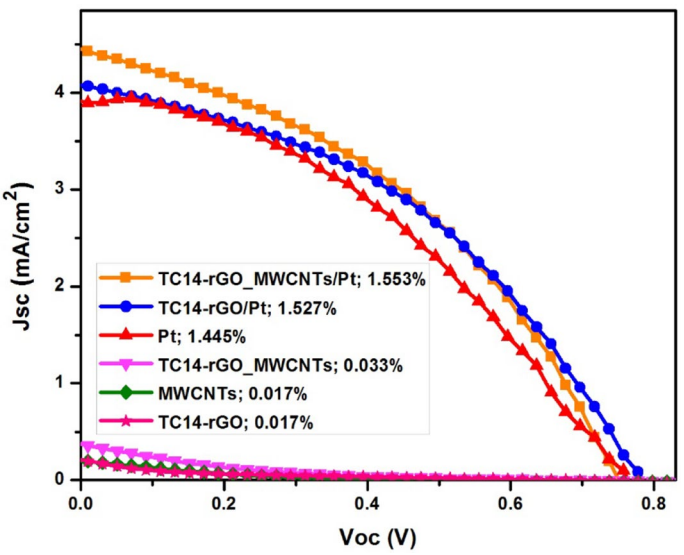

Fig. 9 Solar simulator measurements of DSSCs based on TiO_2 NWs/TiO_2 NPs as photoanodes and various CE thin films

higher η (1.553%) than that of TC14-rGO/Pt (1.527%). The higher J_{SC} values of TC14-rGO_MWCNTs/Pt (4.424 mA/cm^2) and TC14-rGO/Pt (4.096 mA/cm^2) than that of pristine Pt (3.974 mA/cm^2) showed the improved catalytic activity on TC14-rGO_MWCNTs/Pt and TC14-rGO/Pt CE thin films. This result was attributed to the high electron transfer rate at electrolyte and CE interface, which was probably caused by the high conductivity and high surface area of TC14-rGO and TC14-rGO_MWCNTs. The remaining oxygen functional groups from chemical reduction and the defect on TC14-rGO film (indicated by high I_D/I_G ratio of micro-Raman spectra) caused by oxidation and reduction process helped in the reduction reaction of triiodide ion on electrolyte. Fast reduction reaction increases the catalytic activity of the film and consequently increases the DSSCs efficiency [6, 20]. Moreover, the large surface area due to the small size and uniform distribution of Pt NPs coated on TC14-rGO and TC14-rGO_MWCNTs films increases the number of catalytically active sites of the film [16, 20], which provides an advantage in the electron transfer. The closed attachment of Pt on TC14-rGO and TC14-rGO_MWCNTs decreased the interfacial resistance between them, which resulted in the fast electron movement to complete one cycle of DSSCs process. The V_{OC} and FF values of TC14-rGO_MWCNTs/Pt (0.731 V and 40.3) were lower than those of TC14-rGO/Pt (0.784 V and 41.9). V_{OC} and FF displayed insignificant role in the η increment compared with that of J_{SC}. Thus, the highest η was still achieved by TC14-rGO_MWCNTs/Pt CE film. The DSSCs photovoltaic performance is summarised in Table 5.

The photoanode morphology is also crucial in the DSSCs efficiency improvement. The utilisation of mixed-phase TiO_2 NWs/TiO_2 NPs significantly affected the DSSCs photovoltaic performance. This effect was due to high dye adsorption, which was promoted by porous and large surface area of TiO_2 NPs as the upper layer of photoanode. Many excited electrons were obtained after illumination, which increased the J_{SC} value. The linked TiO_2 NPs shown on FESEM images and the optimised TiO_2 NPs thickness (~ 12 μm) prevented the recombination rates and reduced the electron diffusion length, thereby accelerating the electron transfer through the photoanode film [4]. This result was supported by the morphology and perpendicular direction of TiO_2 NWs, which offer the direct and fast electron transport pathway [5, 44, 74, 75] due to the shorter electron transfer rate on TiO_2 NWs than that on TiO_2 NPs. TiO_2 NWs also provide high light scattering ability, which further enhances the electron excitation [5]. The closely adhered TiO_2 NPs on TiO_2 NWs boundary results in low electrical resistance between the two layers [76], which increases the conductivity, as evidenced with the low E_g value of the fabricated photoanode film.

Further EIS analysis was done in order to obtain the series resistance (R_s), charge transfer resistance (R_{ct}), and electron lifetime (τ_n) of the fabricated DSSCs. Based on the inset picture shown in Fig. 10a, the lowest R_s value (70.3 Ω) was achieved by TC14-rGO_MWCNTs/Pt, indicates the fastest interfacial electron transfer which proven to give the highest η (1.553%) among others CE thin film [77]. The semicircle diameter at high frequency region (> 1 kHz) represents the R_{ct} value which related to charge transfer resistance at CE and electrolyte interface. The lowest R_{ct} value (20 kΩ) was achieved by Pt, which can be easily understood due to its excellent electrocatalytic activity. However, solar simulator measurement shows lower Pt efficiency (1.445%) as compared to TC14-rGO/Pt (1.527%) and TC14-rGO_MWCNTs/Pt (1.553%) CE thin films. This was believed due to the highest R_s value of Pt (84.1 Ω) thus slightly decreased the DSSCs performance. The obtained R_s and R_{ct} values of the fabricated DSSCs are summarised in Table 6. Further investigation based on Bode phase plots (Fig. 10b) shows shifted phase peak towards lower frequency region, suggesting longer τ_n which prevented the electron recombination thus improves DSSC performance of produced TC14-rGO_MWCNTs/Pt film [78–81].

Table 5 Photocurrent density–voltage characteristic curves of DSSCs fabricated by using TiO_2 NWs/TiO_2 NPs as photoanodes and various CE thin films

CE thin films	V_{OC} (V)	J_{SC} (mA/cm^2)	FF (%)	η (%)
TC14-rGO_MWCNTs/Pt	0.731	4.424	40.3	1.553
TC14-rGO/Pt	0.784	4.096	41.9	1.527
Pt	0.758	3.974	38.8	1.445
TC14-rGO_MWCNTs	0.752	0.330	11.3	0.033
MWCNTs	0.441	0.201	16.4	0.017
TC14-rGO	0.687	0.214	9.8	0.017

3.7 Electron transfer mechanism

The electron transfer mechanism through fabricated DSSCs is illustrated in Fig. 11. Illumination was performed from the back side of photoanode layer (1) to maximise the harvesting light efficiency, which was also supported by the high transmittance of FTO substrate. The incident light directly reached the dyed TiO_2 layer. TiO_2 NWs achieved higher harvesting light efficiency than that of TiO_2 NPs. The dye molecules attached on TiO_2 NPs and/or TiO_2 NWs are excited electron from the highest occupied molecular orbitals to the lowest unoccupied molecular orbital in around 60 ns [76]. The excited electrons are subsequently injected into the conduction band of TiO_2 NPs and/or TiO_2 NWs, which further oxidises the dye (2). In the present work, a high amount of excited electrons may have resulted from the thickness and large surface area of TiO_2 NPs, which can adsorb more dye molecules than those

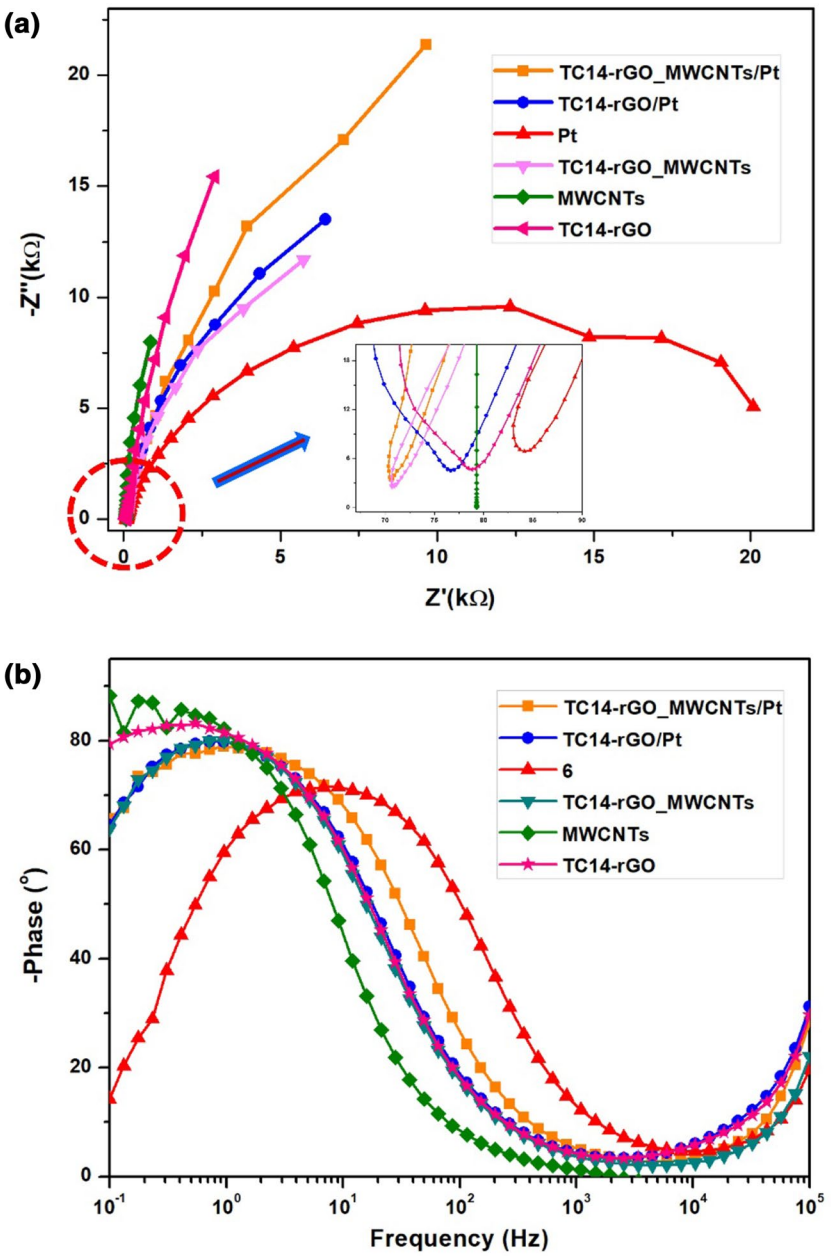

Fig. 10 EIS analysis of DSSCs based on TiO_2 NWs/TiO_2 NPs as photoanodes and various CE thin films

Table 6 EIS analysis of DSSCs fabricated by using TiO_2 NWs/TiO_2 NPs as photoanodes and various CE thin films

CE thin films	R_s (Ω)	R_{ct} (kΩ)
TC14-rGO_MWCNTs/Pt	70.3	47.4
TC14-rGO/Pt	76.6	46.9
Pt	84.1	20.0
TC14-rGO_MWCNTs	70.7	35.6
MWCNTs	79.3	82
TC14-rGO	78.9	90

of TiO_2 NWs. The low amount of dye molecules adsorbed on TiO_2 NWs was compensated with the high harvesting light efficiency due to the closeness of TiO_2 NWs to the FTO substrate and its rough surface, which enhanced the light scattering. The excited electrons in TiO_2 NPs move by hopping through particles (103−106 times between particles) due to their morphology and finally reach the TiO_2 NWs (3) [76]. The TiO_2 NPs closely stacked on TiO_2 NWs without any gap, as shown in FESEM images (Fig. 2e), helped the electrons move fast to TiO_2 NWs due to the low resistance. In addition, the vertically aligned TiO_2 NWs were further accelerated, which provided a direct path for electron movement to the FTO substrate. The collected electrons on photoanode FTO

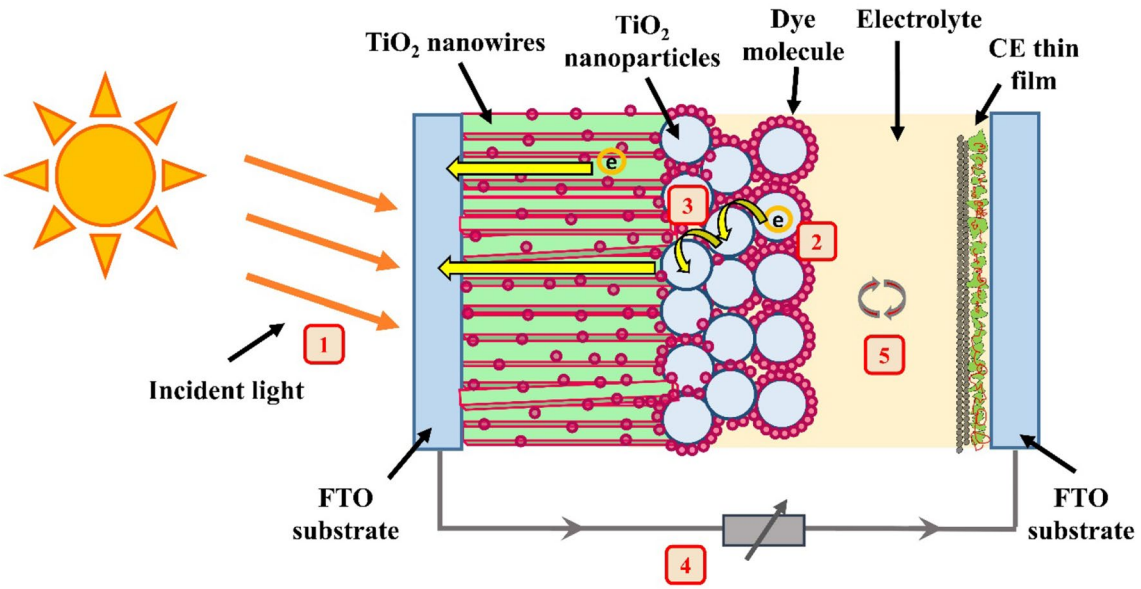

Fig. 11 Schematic diagram of DSSCs electron transfer mechanism based on TiO_2 NWs/TiO_2 NPs as photoanodes and various CE thin films

substrate moved to the FTO substrate of CE thin film (4) and finally reached the electrolyte. The CE thin film morphology further determined the J_{SC} value due to its role in facilitating electrons to the electrolyte. The high conductivity of CE thin film accelerated the electron transfer to the electrolyte, which was used for redox reaction, and regenerated the oxidised dye after electron excitation (5). The thin layer and crumpled-tissue-like morphology of TC14-rGO increase the electrolyte diffusibility, which consequently enhances the redox reaction [13, 14]. This result was also supported by the large surface area and high electrocatalytic activity of Pt NPs and high conductivity of MWCNTs. Less Pt aggregation and small particle size decrease the resistance and offer highly active surface area, which results in efficient electrocatalytic I_3^- reduction in electrolyte [6]. Fast electron transfer was also promoted by the MWCNTs, which connected each TC14-rGO layer. This was supported by EIS analysis which presents low R_s (70.3 Ω) and R_{ct} (47.4 kΩ) value of TC14-rGO_MWCNTs/Pt which indicate the decreased of electron recombination rate thus promotes facile, higher electrons movement, and relatively longer electron lifetime for efficient DSSCs perfomance of TC14-rGO_MWCNTs/Pt CE thin film [82, 83]. This electron transfer process continued in cycle. Thus, the current flew through the circuit.

4 Conclusions

Hybrid CE thin film was successfully fabricated by mixing TC14-rGO produced from chemical reduction process by utilising hyperbranched TC14 surfactant and MWCNTs synthesised from waste palm oil. The TC14-rGO_MWCNTs/Pt thin film was used as CE for DSSCs application. This film yielded the highest η (1.553%) among various CE thin films. The η of this film was 7.5% higher than that of pure Pt CE thin film when mixed-phase TiO_2 NWs/TiO_2 NPs were used as photoanodes. Result confirmed that the utilisation of TC14-rGO_MWCNTs hybrid significantly improved the DSSCs photovoltaic performance. TC14 surfactant stabilised and prevented rGO agglomeration. Consequently, the TC14-rGO_MWCNTs increased the active site areas and enhanced the film conductivity. Therefore, Pt consumption can be minimised by decreasing the Pt coating thickness, thereby lowering the Pt usage in future works.

Acknowledgements The authors would like to express their appreciation to the TWAS-COMSTECH Joint Research Grant (Grant Code: 2017-0001-102-11) and Fundamental Research Grant Scheme (Grant Code: 2015-0154-102-02) for their financial support.

References

1. B. O'Regan, M. Grätzel, A low-cost, high-efficiency solar-cell based on dye-sensitized colloidal TiO_2 films. Nature **353**, 737–740 (1991)
2. D. Qin, Y. Bi, X. Feng et al., Hydrothermal growth and photoelectrochemistry of highly oriented, crystalline anatase TiO_2 nanorods on transparent conducting electrodes. Chem. Mater. **27**, 4180–4183 (2015)
3. M.K. Ahmad, K. Murakami, Rutile-phased TiO_2 nanorods/nanoflowers based dye-sensitized solar cell. Appl. Mech. Mater. **773–774**, 725–728 (2015)

4. J.K. Tsai, W.D. Hsu, T.C. Wu et al., Effect of compressed TiO_2 nanoparticle thin film thickness on the performance of dye-sensitized solar cells. Nanoscale Res. Lett. **8**, 1–6 (2013)
5. W. Wu, J. Liao, H. Chen et al., Dye-sensitized solar cells based on a double layered TiO_2 photoanode consisting of hierarchical nanowire arrays and nanoparticles with greatly improved photovoltaic performance. J. Mater. Chem. **22**, 18057–18062 (2012)
6. M.Y. Song, K.N. Chaudhari, J. Park et al., High efficient Pt counter electrode prepared by homogeneous deposition method for dye-sensitized solar cell. Appl. Energy **100**, 132–137 (2012)
7. A. Yella, H.-W. Lee, H.N. Tsao et al., Porphyrin-sensitized solar cells with cobalt (II/III) based redox electrolyte exceed 12 percent efficiency. Science **80**, 629–634 (2011)
8. E. Ramasamy, W.J. Lee, D.Y. Lee, J.S. Song, Spray coated multi-wall carbon nanotube counter electrode for tri-iodide (I_3^-) reduction in dye-sensitized solar cells. Electrochem. Commun. **10**, 1087–1089 (2008)
9. R. Cruz, D.A.T. Pacheco, A. Mendes, Reduced graphene oxide films as transparent counter-electrodes for dye-sensitized solar cells. Sol. Energy **86**, 716–724 (2012)
10. L.A. Dobrzański, M.P. Prokopowicz, A. Drygała et al., Carbon nanomaterials application as a counter electrode for dye-sensitized solar cells. Arch. Met. Mater. **62**, 27–32 (2017)
11. L. Qiu, H. Zhang, W. Wang et al., Effects of hydrazine hydrate treatment on the performance of reduced graphene oxide film as counter electrode in dye-sensitized solar cells. Appl. Surf. Sci. **319**, 339–343 (2014)
12. Z. Li, M.S. Akhtar, J.H. Kuk et al., Graphene application as a counter electrode material for dye-sensitized solar cell. Mater. Lett. **86**, 96–99 (2012)
13. A.B. Suriani, M.D. Nurhafizah, A. Mohamed et al., Enhanced photovoltaic performance using reduced graphene oxide assisted by triple-tail surfactant as an efficient and low-cost counter electrode for dye-sensitized solar cells. Opt.-Int. J. Light Electron Opt. **139**, 291–298 (2017)
14. A.B. Suriani, M. Muqoyyanah, A. Mohamed et al., Improving the photovoltaic performance of DSSCs using a combination of mixed-phase $_{TiO2}$ nanostructure photoanode and agglomerated free reduced graphene oxide counter electrode assisted with hyperbranched surfactant. Opt.-Int. J. Light Electron Opt. **158**, 522–534 (2018)
15. K. Xu, Y. Shen, Z. Zhang et al., The influence of different modified graphene on property of DSSCs. Appl. Surf. Sci. **362**, 477–482 (2016). https://doi.org/10.1016/j.apsusc.2015.09.265
16. J.H. Kang, T. Kim, J. Choi et al., The hidden second oxidation step of hummers method the hidden second oxidation step of Hummers method. Chem. Mater. **28**, 756–764 (2016)
17. P. Yu, S.E. Lowe, G.P. Simon, Y.L. Zhong, Electrochemical exfoliation of graphite and production of functional graphene functional graphene. Curr. Opin. Colloid Interface Sci. **20**, 329–338 (2015)
18. W. Wu, C. Zhang, S. Hou, Electrochemical exfoliation of graphene and graphene-analogous 2D nanosheets. J. Mater. Sci. **52**, 10649–10660 (2017)
19. M. Yeh, L. Lin, C. Sun et al., Multiwalled carbon annotube@ reduced graphene oxide nanoribbon as the counter electrode for dye-sensitized solar cells. J. Phys. Chem. **118**, 16626–16634 (2014)
20. R. Bajpai, S. Roy, P. Kumar et al., Graphene supported platinum nanoparticle counter-electrode for enhanced performance of dye-sensitized solar cells. Appl. Mater. Interfaces **3**, 3884–3889 (2011)
21. A.B. Suriani, A.A. Azira, S.F. Nik et al., Synthesis of vertically aligned carbon nanotubes using natural palm oil as carbon precursor. Mater. Lett. **63**, 2704–2706 (2009)
22. A.B. Suriani, R.M. Nor, M. Rusop, Vertically aligned carbon nanotubes synthesized from waste cooking palm oil. J. Ceram. Soc. Jpn. **65–66**, 963–968 (2010)
23. A.B. Suriani, S. Muhamad, P.S. Mohamad Saad et al., Effect of temperature on the growth of vertically aligned carbon nanotubes from palm oil. Defect Diffus. Forum **312–315**, 900–905 (2011)
24. M.S. Azmina, A.B. Suriani, A.N. Falina et al., Temperature effects on the production of carbon nanotubes from palm oil by thermal chemical vapor deposition method. Nanomater. Synth. Charact. **364**, 359–362 (2012)
25. M.S. Azmina, A.B. Suriani, A.N. Falina et al., Preparation of palm oil based carbon nanotubes at various ferrocene concentration. Nanomater. Synth. Charact. **364**, 408–411 (2012)
26. A.B. Suriani, A.R. Dalila, A. Mohamed et al., Vertically aligned carbon nanotubes synthesized from waste chicken fat. Mater. Lett. **101**, 61–64 (2013)
27. A.B. Suriani, A.R. Dalila, A. Mohamed et al., Fabrication of vertically aligned carbon nanotubes-zinc oxide nanocomposites and their field electron emission enhancement. Mater. Des. **90**, 185–195 (2016)
28. A.B. Suriani, J. Norhafizah, A. Mohamed et al., Scaled-up prototype of carbon nanotube production system utilizing waste cooking palm oil precursor and its nanocomposite application as supercapacitor electrodes. J. Mater. Sci. Mater. Electron **27**, 11599–11605 (2016)
29. A. Mohamed, A.K. Anas, S.A. Bakar et al., Preparation of multiwall carbon nanotubes (MWCNTs) stabilised by highly branched hydrocarbon surfactants and dispersed in natural rubber latex nanocomposites. Colloid Polym. Sci. **292**, 3013–3023 (2014)
30. A. Mohamed, A.K. Anas, S.A. Bakar et al., Enhanced dispersion of multiwall carbon nanotubes in natural rubber latex nanocomposites by surfactants bearing phenyl groups. J. Colloid Interface Sci. **455**, 179–187 (2015)
31. A.B. Suriani, M.D. Nurhafizah, A. Mohamed et al., A facile one-step method for graphene oxide/natural rubber latex nanocomposite production for supercapacitor applications. Mater. Lett. **161**, 665–668 (2015)
32. A.B. Suriani, M.D. Nurhafizah, A. Mohamed et al., Highly conductive electrodes of graphene oxide/natural rubber latex-based electrodes by using a hyper-branched surfactant. Mater. Des. **99**, 174–181 (2016)
33. V.H. Pham, T.V. Cuong, S.H. Hur et al., Fast and simple fabrication of a large transparent chemically-converted graphene film by spray-coating. Carbon N. Y. **48**, 1945–1951 (2010)
34. M. Quintana, T. Edvinsson, A. Hagfeldt, G. Boschloo, Comparison of dye-sensitized ZnO and TiO_2 Solar cells: studies of charge transport and carrier lifetime. J. Phys. Chem. C **111**, 1035–1041 (2007)
35. P. Tiwana, P. Docampo, M.B. Johnston et al., Electron mobility and injection dinamics in mesoporous ZnO, SnO_2, and TiO_2 Films used in dye-sensitized solar cells. ACS Nano **5**, 5158–5166 (2011)
36. A.K. Chandiran, M. Abdi-jalebi, M.K. Nazeeruddin, M. Gratzel, Analysis of electron transfer properties of ZnO and TiO_2 photoanodes for dye-sensitized solar cells. ACS Nano **8**, 2261–2268 (2014)
37. M.K. Ahmad, S.M. Mokhtar, C.F. Soon et al., Raman investigation of rutile-phased TiO_2 nanorods/nanoflowers with various reaction times using one step hydrothermal method. J. Mater. Sci. Mater. Electron **27**, 7920–7926 (2016)
38. J. Hu, J. Cheng, S. Tong et al., Dye-sensitized solar cells based on P25 nanoparticles/TiO_2 nanotube arrays/hollow TiO_2 boxes three-layer composite film. J. Mater. Sci. Mater. Electron **27**, 5362–5370 (2016)
39. A.Q.D. Faisal, Synthesis and characteristics study of TiO_2 nanowires and nanoflowers on FTO/glass and glass substrates

via hydrothermal technique. J. Mater. Sci. Mater. Electron **26**, 317–321 (2015)
40. S. Sadhu, P. Poddar, Template-free fabrication of highly-oriented single-crystalline 1D-rutile TiO_2-MWCNT composite for enhanced photoelectrochemical activity. J. Phys. Chem. C **118**, 19363–19373 (2014)
41. A. Yasin, F. Guo, G.P. Demopoulos, Aqueous, screen-printable paste for fabrication of mesoporous composite anatase-rutile TiO_2 nanoparticle thin films for (photo)electrochemical devices. ACS Sustain. Chem. Eng. **4**, 2173–2181 (2016)
42. M.K. Ahmad, M. Kenji, Effect of anatase TiO_2 overlayer on the photovoltaic properties of rutile phase nanostructured dye-sensitized solar cell. Micro Nanoelectron **2**, 262–264 (2013)
43. D. Zhang, T. Yoshida, T. Oekermann et al., Room-temperature synthesis of porous nanoparticulate TiO_2 films for flexible dye-sensitized solar cells. Adv. Funct. Mater. **16**, 1228–1234 (2006)
44. A. Kumar, A.R. Madaria, C. Zhou, Growth of aligned single-crystalline rutile TiO_2 nanowires on arbitrary substrates and their application in dye-sensitized solar cells. J. Phys. Chem. C **114**, 7787–7792 (2010)
45. M.Y. Liao, L. Fang, C.L. Xu, F. Wu, Q.L. Huang, M. Saleem, Effect of seed layer on the growth of rutile TiO_2 nanorod arrays and their performance in dye-sensitized solar cells. Mater. Sci. Semicond. Process. **24**, 1–8 (2014)
46. J. Zhou, B. Song, G. Zhao et al., TiO_2 nanorod arrays sensitized with CdS quantum dots for solar cell applications: effects of rod geometry on photoelectrochemical performance. Appl. Phys. A Mater. Sci. Process. **107**, 321–331 (2012)
47. X. Fang, T. Ma, G. Guan et al., Effect of the thickness of the Pt film coated on a counter electrode on the performance of a dye-sensitized solar cell. J. Electroanal. Chem. **570**, 257–263 (2004)
48. L.H. Chang, C.K. Hsieh, M.C. Hsiao et al., A graphene-multi-walled carbon nanotube hybrid supported on fluorinated tin oxide as a counter electrode of dye-sensitized solar cells. J. Power Sources **222**, 518–525 (2013)
49. S.H. Aboutalebi, A.T. Chidembo, M. Salari et al., Comparison of GO, GO/MWCNTs composite and MWCNTs as potential electrode materials for supercapacitors. Energy Environ. Sci. **4**, 1855–1865 (2011)
50. R.J. Meier, Vibrational spectroscopy: a "vanishing" discipline? Chem. Soc. Rev. **34**, 743–752 (2005)
51. Z. Luo, A.S. Poyraz, C. Kuo et al., Crystalline mixed phase (anatase/rutile) mesoporous titanium dioxides for visible light photocatalytic activity. Chem. Mater. **27**, 6–17 (2015)
52. M.M. Yusoff, M.H. Mamat, M.F. Malek et al., Growth of titanium dioxide nanorod arrays through the aqueous chemical route under a novel and facile low-cost method. Mater. Lett. **164**, 294–298 (2016)
53. S.M. Mokhtar, M.K. Ahmad, C.F. Soon et al., Fabrication and characterization of rutile-phased titanium dioxide (TiO_2) nanorods array with various reaction times using one step hydrothermal method. Opt.-Int. J. Light Electron Opt. **154**, 510–515 (2018)
54. J. Yan, G. Wu, N. Guan et al., Understanding the effect of surface/bulk defects on the photocatalytic activity of $_{TiO2}$: anatase versus rutile. Phys. Chem. Chem. Phys. **15**, 10978 (2013)
55. N. Liu, F. Luo, H. Wu et al., One-step ionic-liquid-assisted electrochemical synthesis of ionic-liquid-functionalized graphene sheets directly from graphite. Adv. Funct. Mater. **18**, 1518–1525 (2008)
56. J. Zhao, J. Wu, M. Zheng et al., Improving the photovoltaic performance of dye-sensitized solar cell by graphene/titania photoanode. Electrochim. Acta **156**, 261–266 (2015)
57. A. Ambrosi, M. Pumera, Electrochemically exfoliated graphene and graphene oxide for energy storage and electrochemistry applications. Chem. Eur. J. **22**, 153–159 (2016)
58. H. Wang, Y. Wang, X. Cao et al., Vibrational properties of graphene and graphene layers. J. Raman Spectrosc. **40**, 1791–1796 (2009)
59. M. Zhou, J. Tang, Q. Cheng et al., Few-layer graphene obtained by electrochemical exfoliation of graphite cathode. Chem. Phys. Lett. **572**, 61–65 (2013)
60. C.K. Chua, M. Pumera, Chemical reduction of graphene oxide: a synthetic chemistry viewpoint. Chem. Soc. Rev. **43**, 291–312 (2014)
61. K.H. Lee, B. Lee, S.-J. Hwang et al., Large scale production of highly conductive reduced graphene oxide sheets by a solvent-free low temperature reduction. Carbon N. Y. **69**, 327–335 (2014)
62. J.H. Lehman, M. Terrones, E. Mansfield et al., Evaluating the characteristics of multiwall carbon nanotubes. Carbon N. Y. **49**, 2581–2602 (2011)
63. S. Costa, E. Borowiak-Palen, M. Kruszynska et al., Characterization of carbon nanotubes by Raman spectroscopy. Mater. Sci. **26**, 432–441 (2008)
64. C. Wu, Z. Wang, L. Wang, P.T. Williams, J. Huang, Sustainable processing of waste plastics to produce high yield hydrogen-rich synthesis gas and high quality carbon nanotubes. RSC Adv. **2**, 4045–4047 (2012)
65. L. Bokobza, J. Zhang, Raman spectroscopic characterization of multiwall carbon nanotubes and of composites. Express Polym. Lett. **6**, 601–608 (2012)
66. J. Shao, W. Lv, Q. Guo, C. Zhang, Q. Xu, Q. Yang, F. Kang, Hybridization of graphene oxide and carbon nanotubes at the liquid/air interface. Chem. Commun. **48**, 3706–3709 (2012)
67. U. Yaqoob, A.I. Uddin, G.-S. Chung, A high-performance flexible NO_2 sensor based on WO_3 NPs decorated on MWCNTs and RGO hybrids on PI/PET substrates. Sens. Actuat. B Chem. **224**, 738–746 (2016)
68. L. Wan, Q. Zhang, S. Wang et al., A two-step reduction method for synthesizing graphene nanocomposites with a low loading of well-dispersed platinum nanoparticles for use as counter electrodes in dye-sensitized solar cells. J. Mater. Sci. **50**, 4412–4421 (2015)
69. G. Yue, J. Wu, Y. Xiao et al., Platinum/graphene hybrid film as a counter electrode for dye-sensitized solar cells. Electrochim. Acta **92**, 64–70 (2013)
70. J. Lei, H. Li, J. Zhang, M. Anpo, Mixed-Phase TiO2 Nanomaterials as Efficient Photocatalysts. Low Dimensional and Nanostructured Materials and Devices. (Springer, Switzerland, 2016), pp. 423–429
71. Q. Zhang, Y. Liu, Y. Duan, N. Fu, Q. Liu, Y. Fang, Q. Sun, Y. Lin, Mn_3O_4/graphene composite as counter electrode in dye-sensitized solar cells. RSC Adv. **4**, 15091–15097 (2014)
72. S. Hwang, M. Batmunkh, M.J. Nine, H. Chung, H. Jeong, Dye-sensitized solar cell counter electrodes based on carbon nanotubes. ChemPhysChem **16**, 53–65 (2015)
73. T. Adachi, H. Hoshi, Preparation and characterization of Pt/carbon counter electrodes for dye-sensitized solar cells. Mater. Lett. **94**, 15–18 (2013)
74. X. Feng, K. Zhu, A.J. Frank, C.A. Grimes, T.E. Mallouk, Rapid charge transport in dye-sensitized solar cells made from vertically aligned single-crystal rutile TiO_2 nanowires. Angew. Chem. **124**, 2781–2784 (2012)
75. J. Su, L. Guo, High aspect ratio TiO_2 nanowires tailored in concentrated HCl hydrothermal condition for photoelectrochemical water splitting. RSC Adv. **5**, 53012–53018 (2015)
76. L. Kosyachenko, *Solar Cells-Dye-Sensitized Devices* (Intech, Croatia, 2011)
77. A.M. Ilyas, M.A. Gondal, U. Baig et al., Photovoltaic performance and photocatalytic activity of facile synthesized graphene decorated TiO_2 monohybrid using nanosecond pulsed ablation in liquid technique. Sol. Energy **137**, 246–255 (2016)

78. J. Chou, C. Huang, Y. Lin et al., The influence of different annealing temperatures on graphene modified TiO_2 for dye-sensitized solar cell. IEEE Trans Nanotechnol **15**, 164–170 (2016)
79. J. Tian, R. Gao, Q. Zhang et al., Enhanced performance of CdS/CdSe quantum dot cosensitized solar cells via homogeneous distribution of quantum dots in TiO_2 film. J. Phys. Chem. C **116**, 18655–18662 (2012)
80. S. Sarker, A.J.S. Ahammad, H.W. Seo, D.M. Kim, Electrochemical impedance spectra of dye-sensitized solar cells: fundamentals and spreadsheet calculation. Int. J. Photoenergy (2014). https://doi.org/10.1155/2014/851705
81. S.P. Lim, A. Pandikumar, H.N. Lim et al., Boosting photovoltaic performance of dye-sensitized solar cells using silver nanoparticle-decorated N,S-Co-doped-TiO_2 photoanode. Sci. Rep. **5**(119), 1–14 (2015)
82. D. Dahlan, S.K. Md Saad, A.U. Berli et al., Synthesis of two-dimensional nanowall of Cu-Doped TiO_2 and its application as photoanode in DSSCs. Phys. E Low-Dimens. Syst. Nanostruct. **91**, 185–189 (2017)
83. A.A. Umar, S. Nafisah, S.K. Md Saad et al., Poriferous microtablet of anatase TiO_2 growth on an ITO surface for high-efficiency dye-sensitized solar cells. Sol. Energy Mater. Sol. Cells **122**, 174–182 (2014)